Nafar Dastgerdi, Jairan; Jaberi, Omid; Remes, Heikki; Lehto, Pauli; Hosseini Toudeshky, Hossein; Kuva, Jukka

Fatigue damage process of additively manufactured 316 L steel using X-ray computed tomography imaging

Published in:
Additive Manufacturing

DOI:
10.1016/j.addma.2023.103559

Published: 25/05/2023

Document Version
Publisher's PDF, also known as Version of record

Please cite the original version:
Nafar Dastgerdi, J., Jaberi, O., Remes, H., Lehto, P., Hosseini Toudeshky, H., & Kuva, J. (2023). Fatigue damage process of additively manufactured 316 L steel using X-ray computed tomography imaging. *Additive Manufacturing*, *70*, Article 103559. https://doi.org/10.1016/j.addma.2023.103559

Additive Manufacturing 70 (2023) 103559

Contents lists available at ScienceDirect

Additive Manufacturing

journal homepage: www.elsevier.com/locate/addma

Fatigue damage process of additively manufactured 316 L steel using X-ray computed tomography imaging

Jairan Nafar Dastgerdi [a,b,*], Omid Jaberi [a], Heikki Remes [b], Pauli Lehto [b], Hossein Hosseini Toudeshky [a], Jukka Kuva [c]

[a] Department of Aerospace Engineering, Amirkabir University of Technology (Tehran Polytechnic), 424 Hafez Avenue, Tehran, Iran
[b] Department of Mechanical Engineering, School of Engineering, Aalto University, P.O. Box 14300, FIN-00076 Aalto, Finland
[c] Circular Economy Solutions, Geological Survey of Finland, Vuorimiehentie 2 K, FIN-02150 Espoo, Finland

ARTICLE INFO

Keywords:
Additive manufacturing
Defect
X-ray computed tomography
Fatigue crack growth prediction
Stainless steel 316 L

ABSTRACT

Failure under cyclic loading in the presence of manufacturing defects is a substantial risk for additively manufactured (AM) metal components. This study aims to clarify the correlation between process-related defects (internal pores and surface roughness) and fatigue performance of AM 316 L stainless steel. X-ray computed tomography (XCT) has been employed to characterize process-related defects' features and their synergistic interaction to define the effective defect size parameter $\sqrt{area_{eff}}$, leading to identifying potential sites for fatigue crack initiation before testing. Then, the defects' growth is monitored using XCT imaging under cyclic loading to provide further insight into the fatigue damage process of AM stainless steels. A novel characterization framework is developed for monitoring the fatigue crack initiation and propagation based on measuring the variation in specimen surface topography in the axial and circumferential directions. Moreover, a fracture-mechanics based analytical framework is developed for the fatigue life prediction of AM components while the progression of the aspect ratio of semi-elliptical surface crack during its growth is considered. It is found that a significant fraction of the fatigue life is consumed for crack initiation and the damage progression dominantly occurs at the predicted maximum equivalent defect size, which is detected before fatigue testing. Therefore, the critical equivalent defect size can be considered as an initial short crack in the critical defect-based fatigue crack growth model for AM components. The proposed single crack growth model, by applying an appropriate characterization approach to detect the initial semi-elliptic surface short crack based on defects' features and their interaction, demonstrates promise to be suited as an engineering approach for fatigue life prediction of AM components. This model shows a good correlation between XCT imaging and the predicted crack initiation and propagation phases for the tested AM 316 L stainless steel samples.

1. Introduction

Metal additive manufacturing (AM) is a fast-growing technology appealing to different industrial sectors [1–3], with a keen interest in exploiting the advantages of metal AM components. However, several challenges must be solved before metal AM processes can be fully employed in industrial applications for manufacturing load-carrying components, especially under cyclic loading in fracture-critical applications. The metal AM process includes complicated multi-physics phenomena, making the fabricated components prone to residual stresses and manufacturing defects, e.g., pores and high surface roughness [4–8]. Post-heat-treatment and imposing a controlled cooling by pre-heating the platform can mitigate or sensibly reduce detrimental residual stresses [9,10]. There is currently significant interest in understanding the influence of process-induced defects and heterogeneous microstructure on the structural integrity of metal additive manufactured (AM) parts, especially in fatigue-critical load-carrying applications. Therefore, there is an urgent need for research on the correlation between process-related defects (internal pores and surface roughness) and the fatigue damage mechanisms of metal AM materials under cyclic loading. The fatigue damage process (the crack initiation, fatigue crack growth, and final fracture) of metal AM components is a field of investigation still in its infancy. AM is employed to fabricate components made from various engineering alloys such as Al, Ti, Ni, Mg alloys, and

* Corresponding author at: Department of Aerospace Engineering, Amirkabir University of Technology (Tehran Polytechnic), 424 Hafez Avenue, Tehran, Iran.
E-mail address: jairan.nafardastgerdi@aalto.fi (J. Nafar Dastgerdi).

https://doi.org/10.1016/j.addma.2023.103559
Received 11 January 2023; Received in revised form 5 April 2023; Accepted 13 April 2023
Available online 14 April 2023

steels [11]. Among these, steels have involved about one-third of the metal AM publications in literature [12]. This paper has studied the AM stainless steel 316 L due to its high mechanical strength, corrosion resistance, excellent formability, and weldability, which are crucial in different industries such as automotive, energy, marine, and biomedical.

XCT, as a powerful non-destructive measurement technique, offers the excellent capability to assess heterogeneous materials' microstructure [13,14] three-dimensionally. In most of the previous work, XCT has been employed to characterize the internal defects, e.g., the population, morphology, and dimensions of porosities, as well as the lack of fusion defects of AM components [15–20]. One main benefit of XCT is the capability to resolve the temporal domain, which is particularly useful for measuring deformed components in-situ or ex-situ. In both cases, the inclusion of the temporal domain is named as 4DXCT and provides a powerful tool for identifying the material response and damage progression to different loading conditions. Tammas-Williams et al. [21] employed the 4DXCT to study crack growth from internal defects of AM Ti alloys for the first. Recently, Qian et al. [22] have used the XCT to visualize the fatigue crack front of an AM AlSi10Mg alloy. They performed the XCT in two stages: before fatigue testing and after 300000 cycles when large cracks were expected to have developed. In these studies, the specimen surfaces were machined flat, and thus the influence of surface topography was excluded, and only the growth of cracks from internal pores or near surface pores was investigated. However, surface polishing/machining is not always possible for AM components with complex geometry. Even with surface machining, some near-surface defects connect to the surface, and thus it is not feasible to eliminate the surface roughness effects. Most of the previous investigations demonstrated that the influence of surface roughness is most important for the as-built specimens [23–26]. Therefore, it is crucial to employ powerful methods and analysis approaches to detect and characterize fatigue crack growth from surface defects.

Recently, the authors have introduced a new method to characterize the surface irregularities of metal AM specimens using XCT measurements [27]. This approach overcame the limitations of previous methods, based on stylus surface profilometry results [28], 3D optical profilometry results [29], and XCT results [30–33]. These limitations in the stylus or 3D optical profilometry included overlooking the thin and deep defects which are out of reach in these measuring methods and the inability to measure the surface topography of curved shapes and internal surfaces of complex AM parts, for example, struts in lattices [34]. Although the XCT technique overcame these inabilities and could identify critical features of the surface defects of the metal AM components, e.g., crack-like notches, there was still a gap in the determination algorithm to characterize the surface defects of complex metal AM parts systematically. An example is the notch-based surface roughness evaluation method presented by Plessis and Beretta [35] for XCT imaging of specimens with curved shapes. In this approach, a smooth cylinder geometry element was fitted to the exterior surface of the tested sample before fatigue testing and crack formation to create a duplicate volume of this cylinder. The original surface was compared to the best-fit cylinder volume. Then, the maximum deviation between the rough surface and the fitted cylinder was considered as a "nominal-actual comparison" parameter to define the notches. However, their approach presented local information about the surface defects, mainly focusing on the "killer notches"; this method still has two limitations. First, the connectivity between surface notches depends on the depth of the notches, and therefore a depth criterion for defining the notches as defects depends on the surface condition and is a manual step that the user detects. Second, this approach is primarily employed to visualize and interpret notch geometry relative to crack location. However, they have reported that some killer notches may not be detected using this approach.

It should be noted that the surface profiles for each section have some peaks and valleys, and the deviation from the center (mean) axis should be considered a criterion for notch detection. Nafar Dastgerdi et al. [27] recently introduced a determination algorithm applied to XCT measurements to mathematically calculate the center axis and determine the valleys' notches and depth. Thus, the surface defects of metal AM components could be characterized systematically with the minimum possible error in image processing. Furthermore, holistic information on the surface topologies of AM components was provided using quantitative parameters (e.g., R_a (arithmetic mean roughness) and R_z (the five largest peak-to-peak average roughness)), which could be measured for each surface profile around the sample. In the current study, the surface roughness characterization methodology has been further developed and implemented to measure the surface profiles in the temporal domain during fatigue loading, enabling us to 1) detect fatigue crack initiation and 2) monitor fatigue crack propagation.

Since fatigue cracks initiate from defects, it is crucial to develop analytical approaches to predict fatigue failure for critical practices of metal AM components under cyclic loadings. Fracture mechanics-based methods for defect-based fatigue life prediction of AM components have been of great interest, as discussed extensively in Ref. [36]. Most previous studies have only considered the internal defect size for defect-based modeling and prediction of fatigue strength of metal AM parts [6,22,37–39]. Sanaei and Fatemi [40] have defined an equivalent defect parameter for estimating the initial defect size of metal AM components composed of the maximum prospective internal defect size and the maximum prospective equivalent surface defect size using Murakami's equivalent defect size [41]. However, the interaction effect of internal and surface defects has yet to be considered. They also have assumed an initial semi-elliptical surface defect with a constant aspect ratio for the crack during its growth resulting in a constant geometry factor up to failure. The current study presents a novel analytical framework for defect-based fatigue life prediction of metal AM components, while the above-mentioned limitations of the previous studies have been considered. A single crack propagation model based on the critical equivalent defect size $\sqrt{area_{eff}}$ has been introduced to predict the fatigue crack propagation life. In defect-based fatigue life prediction, the defects are considered as existing small cracks. Thus, it is crucial to calculate the initial effective defect size correctly. In this study, the critical equivalent defect size considers the internal and surface defects and their interactions using the newly introduced 3D defect determination algorithm [27]. Moreover, the proposed critical defect-based fatigue crack growth model takes into account the progress of the crack's aspect ratio during its growth. The introduced defect and damage characterization framework and fatigue life prediction framework have been applied to AM stainless steel 316 L for validation purposes. XCT imaging of tested samples under cyclic loading combined with defect analysis indicates the possibility and tendency of interaction and merging of internal and surface defects during cyclic loading. Furthermore, comparisons have been carried out between the predicted maximum equivalent defect size and the observed fatigue cracks using the $\sqrt{area_{eff}}_{\max}$ parameter. Finally, the comparison of predicted and experimental fatigue life is given, with recommendations for the practical application of the developed framework for the fatigue life prediction of AM components.

2. Material and methods

2.1. Material and specimen fabrication

This study employed direct metal laser sintering as a powder bed fusion method to produce the stainless steel 316 L samples. The test samples were fabricated using the EOS GmbH (M290) system on the same platform in a single build. The powder was spherical and approximately 37 μm in diameter on average. The hourglass-shaped round samples were manufactured vertically with the tensile axis and manufacturing direction parallel to the z-direction; see Fig. 1a-b. No post-process machining was carried out, and all specimens were fabricated to the net shape. Samples were made with a laser power of 250 W

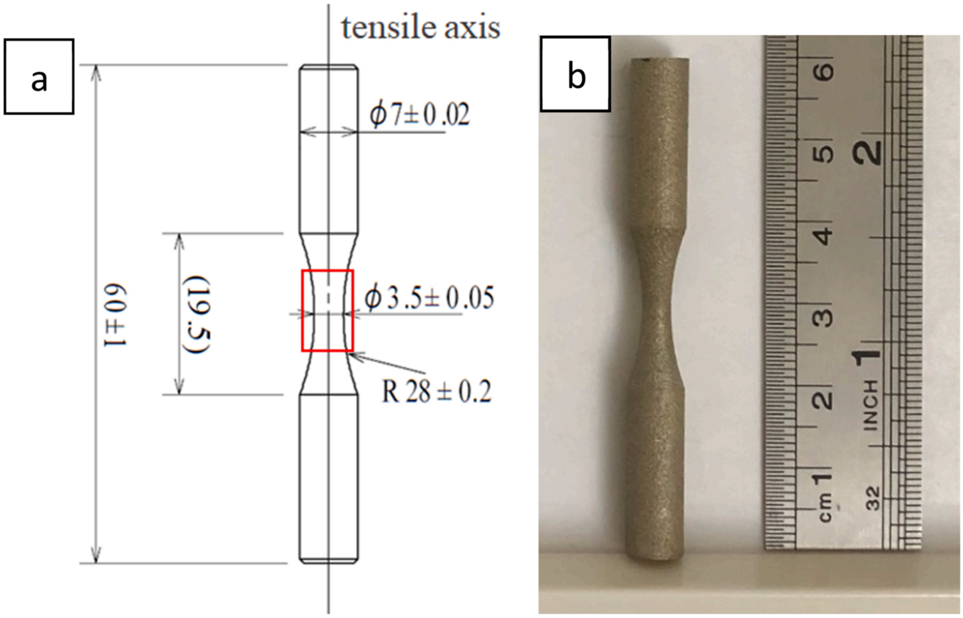

Fig. 1. (a) Geometry and dimensions of the manufactured vertical fatigue specimen. (b) Example of the fabricated specimen. XCT region of interest is marked with a red rectangle. All dimensions are in mm.

and a scanning speed of 1083 mm/s. The hatch distance was 90 μm and the manufacturing layer thickness was 40 μm. The volumetric energy density was computed to be 64.12 J/mm^3 according to equation $E_a = \frac{P}{\nu h t}$ (E_a,P,ν,h,and t are energy density per unit volume (J/mm^3), beam power (W), beam velocity (mm/s), hatch spacing or line offset (mm), and layer thickness (mm)). The platform was pre-heated and kept at a constant 80 °C during the manufacturing process. Heat treatment was not carried out for the samples. Residual stresses are always present in as-built parts. However, in this study, the scanning chessboard island size was small, the platform was pre-heated, and the samples were not deformed after printing, and thus, it can be assumed the residual stress is minor according to the previous experimental investigations; [42–44].

The microhardness and density of the fabricated material were 220 HV (kgf/mm^2) and 7.965 g/cm^3 which are consistent with previous results for AM stainless steel 316 L [45,46], although the manufacturing parameters are different.

2.2. Interrupted fatigue test and XCT imaging

The ex-situ XCT (4DXCT) was carried out to scan the defects (internal and surface) under fatigue loading to detect defects' growth and interaction, i.e., fatigue crack initiation and propagation. The XCT scanning was carried out using General Electric (GE) Phoenix v|tome|x s machine with 5 μm pixel size. The X-ray tube acceleration voltage and power were set to 170 kV and 5.1 W, respectively. To absorb low-energy X-rays, a 0.5 mm copper filter was employed. The distance between layers for each scan was 5μm. Scans were done with a single longitudinal position and a 360° rotation, circular trajectory. Scanning was carried out with 1 s exposure time and by averaging two or three exposures per angular position. The region of interest for XCT imaging was the middle 10 mm of the specimen in the z-direction. This region is highlighted by the red rectangle in Fig. 1.

The 4DXCT was performed for two samples at stress amplitudes of 170 and 190 MPa using load-controlled uniaxial fatigue testing with a load ratio R = 0.1 and a loading frequency of 10 Hz. Due to the uncertainty expected in fatigue, the fatigue pre-tests with three repetitions were carried out before 4DXCT fatigue tests to find an estimate for the average fatigue life of the ordinary XCT samples. Based on the pre-test information the fatigue test interruptions for 4DXCT characterization were chosen. Table 1 shows the total fatigue life for the pretests and the ordinary XCT samples. Both samples 1-XCT and 2-XCT were scanned before any fatigue loading was applied. Then, sample 1-XCT was scanned after around 60% of the initial estimate for the fatigue life,$0.6 \times N_{f,mean}$, at 78,000 cycles. After that, the XCT scans were carried out every 10,000 cycles, with five scans performed in total during the fatigue test. The initial results demonstrated that fatigue crack initiation occurred in 65% of the total life. Thus, for the sample 2-XCT, the fatigue test interruptions and XCT scanning occurred at 62,000 cycles ($\approx 0.65 \times N_{f,mean}$) and 72,000 cycles. To monitor the damage process stages more accurately, the next interruption occurred at 76,000 cycles, and then the sample was scanned at 87,000 cycles. Due to scattering in fatigue testing, the lifetime exceeded the predicted mean fatigue life, with the following scans performed at 95 000 cycles and at 104,003 cycles when the final failure occurred.

2.3. 3D internal defect and surface roughness characterization

The XCT imaging data were analyzed using ThermoFisher PerGeos 2020.2 software to measure internal defects' volume and position. This software used the watershed algorithm for generating data on internal defects volume and position [47]. The internal defects' distribution throughout the specimen along the axis and around it at different radial angles has been investigated. Defects on the surface, usually referred to as surface roughness, are the other type of defects that should be characterized as a rough surface is intrinsic to AM due to the build process's layer-by-layer nature. For this purpose, the new surface defect determination algorithm was employed [27]. In this approach, binarization transformed a gray-level image into a binary image. Then, internal

Table 1
Fatigue life of pre-tests and actual XCT samples at a constant stress amplitude.

Sample 1, $\sigma = 170MPa$	Sample 2, $\sigma = 190MPa$
$N_{f,sample1-1} = 122877$	$N_{f,sample2-1} = 96955$
$N_{f,sample1-2} = 145320$	$N_{f,sample2-2} = 99650$
$N_{f,sample1-3} = 125763$	$N_{f,sample2-3} = 89548$
$N_{f,mean} = 131320$	$N_{f,mean} = 95384$
$N_{f,sample1-XCT} = 131932$	$N_{f,sample2-XCT} = 104003$

defects (pores) were excluded, the edge of the sample was specified, and (X,Y) coordinate pairs on edge were extracted at specific angles around the sample axis. These coordinate pairs were used to generate the sample's axial surface profiles at different radial angles. After determining the (X,Y) coordinate pairs on the edge, the internal defects volume and position data were employed to specify the internal defect's distance from the surface using the K-nearest neighbors algorithm [48]. The internal defects' projected area in the plane transverse to the build direction, their distance from the surface, and the depth of valleys on this plane in the radial direction were chosen as the most important metrics in the current study. They must be characterized to define the effective defect size parameter, considering process-related defects' features and their synergistic interaction.

2.4. Fatigue damage detection

Fatigue crack typically initiates from the sample surface, and defects on the surface are the potential sites for crack initiation, especially in metal AM components. This study proposes a novel characterization framework for detecting fatigue crack initiation and monitoring the fatigue damage process based on measuring the temporal variation of specimen surface topography in the axial (Z) and radial (θ) directions. The detailed process of the proposed approach is depicted in Fig. 2a-c. To accurately determine the initial defects' size and to detect the fatigue crack growth, post-processing of XCT data is required. As shown in Fig. 2a, four image processing steps were carried out for 'as measured' XCT images for every axial cross-section to determine the boundary profile of the specimen. In Step 1, the 'as measured' XCT image contrast is enhanced by changing the dynamic range of measured 8-bit grayscale values for visual representation, providing a clear outer profile for the sample. The exponential intensity transform is used to enhance the details of the bright regions using the gamma expansion operator [49]. In Step 2, images are binarized using a grayscale threshold level of 39, and then all holes in the sample interior have been filled to only focus on the surface-connected defects, representing the current stage of the defected area and crack propagation. This step is carried out using the open-source program ImageJ (Fiji plugin version) [50]. In Step 3, the edge of the binary image is extracted as (X,Y) coordinate pairs, with the edge defined as the outermost 'white' points in the binary data. Because the fatigue cracks grow perpendicular to the loading direction, the

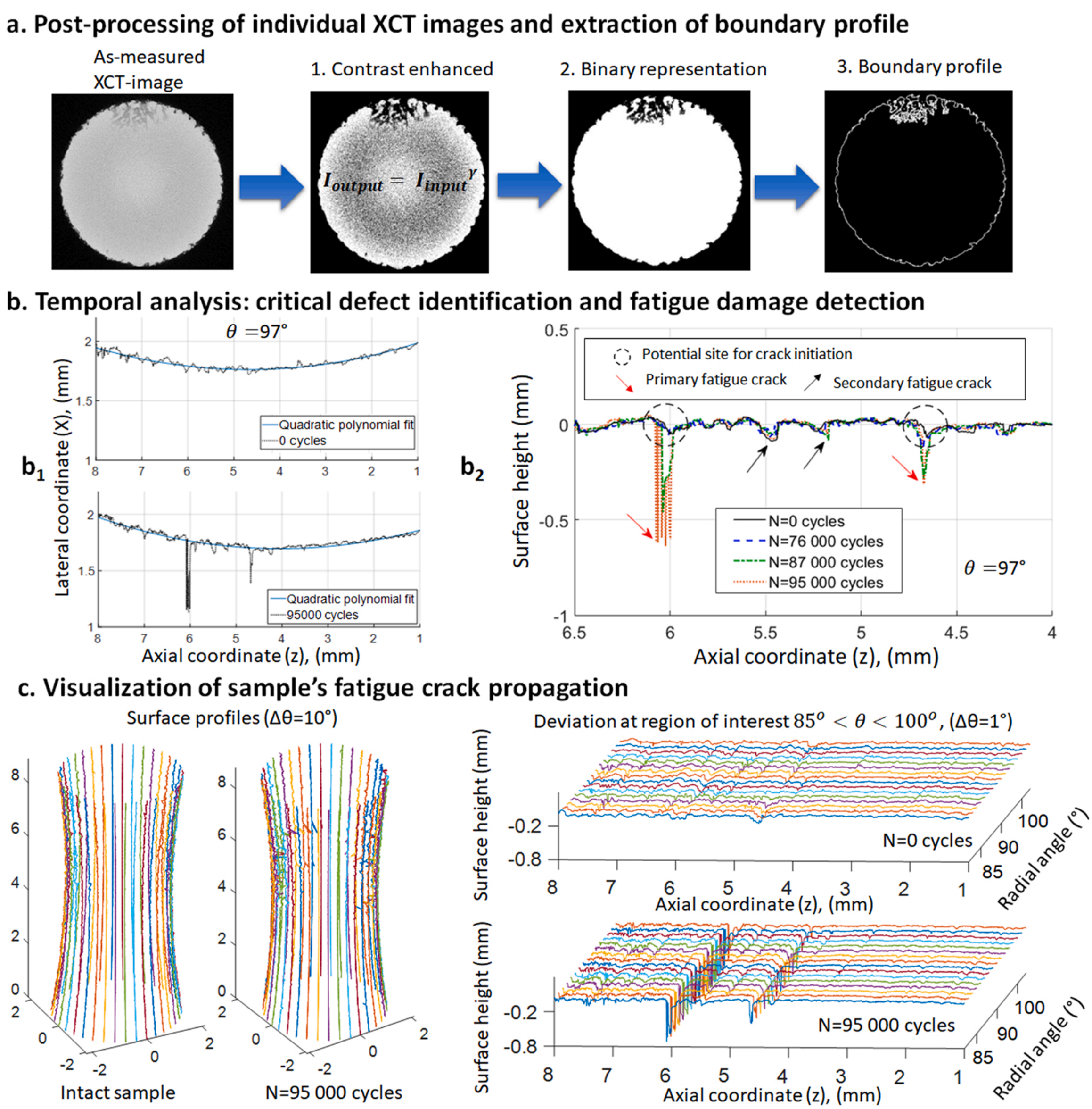

Fig. 2. Schematic of the introduced approach for fatigue damage detection, (a) post image-processing of XCT images to extract boundary profiles, (b) critical defect identification and fatigue damage detection, and (c) visualization of sample's fatigue crack propagation.

coordinate pairs are used to generate the sample's axial surface profiles at each specific radial angle. The axial profiles show the initiation and growth of fatigue cracks as high local gradients, as depicted in Fig 2b$_1$. Finally, the magnitude of deviation for the peaks and valleys of the surface profile from the mean contour of the sample at different angles around the sample is considered as the criterion for surface-connected defects and fatigue crack detection; see Fig. 2b$_2$. To consider the contoured shape of the specimen, the Euclidean distance between the coordinate pairs and the quadratic polynomial fit is used (blue line in Fig. 2b$_1$). The magnitude of deviation for peaks and valleys in the vertical magnification direction from the mean axis, named surface height, is then used to calculate surface roughness, e.g., R_a and R_z. By comparing the magnitudes of these deviations for different XCT scans, fatigue crack propagation under cyclic loading is detected and can be explicitly quantified; see Fig. 2c. In this study, an in-house code is developed using the new proposed characterization approach following the variation of surface profiles to quantitatively investigate the fatigue damage process. Using the proposed approach, the R_a and R_z values for different surface profiles around the sample can be calculated. The average value of R_a for this specimen is 12.6 μm, consistent with other results for AM stainless steel 316 L [51–53], although the manufacturing parameters and measuring approach differ.

3. Critical defect-based fatigue crack growth model

Fatigue life is generally allocated into three stages; nucleation, short crack growth (less than 1 mm), and long crack growth (larger than 1 mm). Together the first two stages are called macro crack initiation, and when it is employed for defect-based life prediction, nucleation life is assumed to be zero, and short crack growth is predominant. For AM metals, the short crack growth behavior is more critical than the long crack growth behavior when using defect-based life prediction methods [41]. Thus, it is crucial first to determine the initial short crack size correctly and second to employ an appropriate crack growth model considering both short and long crack growth regimes. Generally, the Hartman-Schijve variant [54] of the NASGRO equation has the potential to capture the entire crack growth process, especially when defects are small and the initial stress intensity range values are close to the threshold regime.

In the case of metal AM components, crack initiation typically happens at the most critical defect, depending on the stress state at that location [40]. Thus, the proposed fatigue crack model only considers the largest critical effective defect size ($\sqrt{area_{eff}}$) as initial crack size. In the current study, this critical defect is detected from the XCT data of the intact sample, and it is considered as an initial short crack. The interaction effect between internal and surface defects is also considered to account for the detrimental effect of porosity in AM components. Therefore, we introduce the incorporation of internal defects and surface roughness as an effective initial crack size. As defined by Murakami [55], if the space between two adjacent defects (internal and surface) is smaller than the size of the smaller defect, the effective defect size must be assessed by summing the sizes of two defects plus the space between two defects. Thus, we have determined the effective defect size as [27]:

$$\sqrt{area_{eff}} = \sqrt{area_D} + \sqrt{area_R} + d_{R-D} = \sqrt{area_D} + R_v + d_{R-D}. \quad (1)$$

where $\sqrt{area_D}$, $\sqrt{area_R}$ are the prospective internal and equivalent surface roughness defect sizes, respectively. Parameter d_{R-D} is the shortest distance between two adjacent defects. The deepest valley of the surface profile R_v, is an appropriate parameter to be used as the calculated equivalent surface roughness defect size $\sqrt{area_R}$, [27,41,56,57]. This method determines the critical defects using XCT data of the intact sample while the synergistic effects of internal and surface defects on the fatigue performance of metal AM parts have been considered. Fig. 3 shows schematically the process of the introduced approach. First, the roughness of all surface profile is checked around the sample and the 10–15 critical surface profiles with the biggest R_z values are selected. Then, these critical surface profiles are separately checked to find the deepest valleys (R_v). At the corresponding location of the deepest valley in each profile (Z_v), the presence of the internal defect, its projected area ($\sqrt{area_D}$), and its distance from the edge or deep valley (d_{R-D}) are determined to investigate the synergistic effect of the internal and surface defect for considering in the calculation of the critical equivalent defect size, see Eq. (1). To check whether the most critical value occurs at the predicted location of the deepest valley, $\sqrt{area_{eff}}$ is calculated at Z_v in different radial angles for other existing surface and internal defects and the polar distributions of $\sqrt{area_{eff}}$ is inspected, see Step 4 in Fig. 3. This final checking is used for all critical valleys. Thus, it is possible to

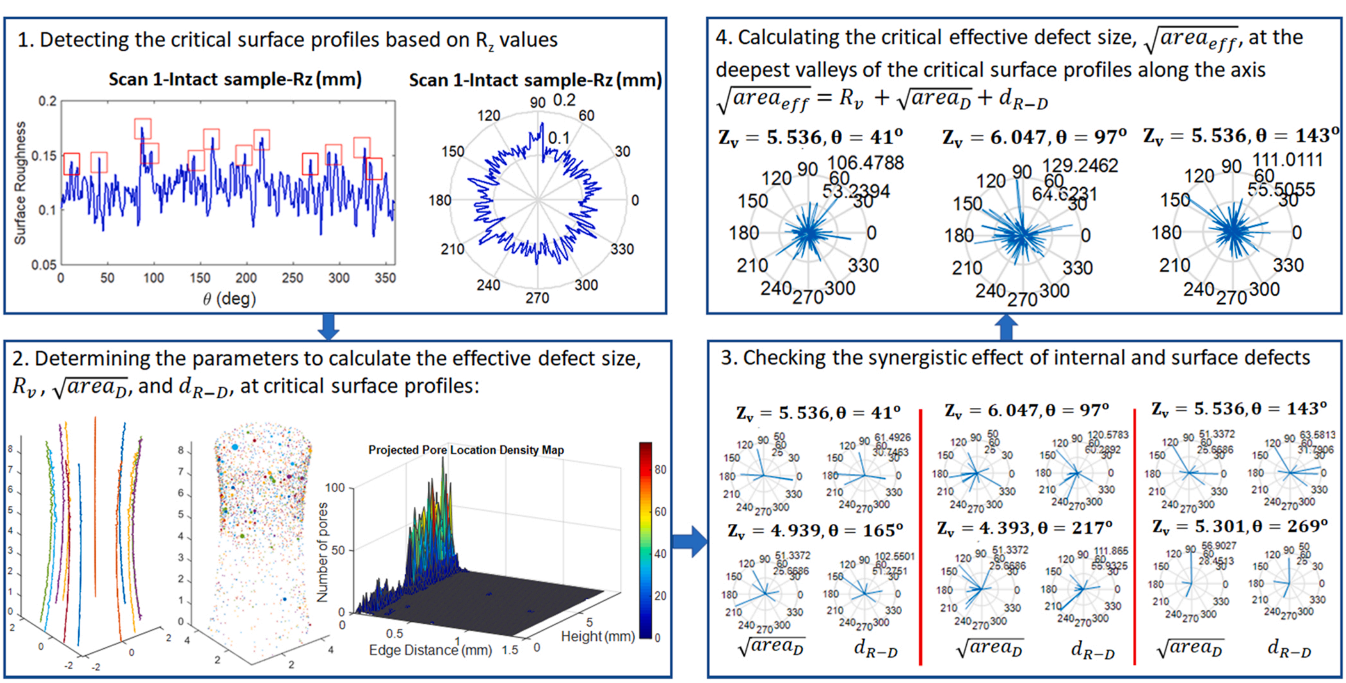

Fig. 3. Schematic of the proposed approach to calculate $\sqrt{area_{eff}}$ (effective initial crack size).

anticipate from which defects identified the failure would originate before the fatigue loading.

After determining the most critical effective defect as an initial short crack size, it can be compared to the threshold small crack size, $\sqrt{area_{th}}$, that represents the transition crack size above which the usual crack growth rate ($\frac{da}{dN}$) versus stress intensity range (ΔK) relationship can be applied. Then, it can be determined whether the initial crack size is physically small and if the stress intensity factor is larger than the threshold value. The relationship between the threshold stress intensity factor, material Vickers hardness and threshold small crack size has been determined by Murakami [55]:

$$\Delta K_{th} = 3.3 \times 10^{-3}(HV + 120)\left(\sqrt{area_{th}}\right)^{\frac{1}{3}}. \tag{2}$$

where HV (kgf/mm^2) is Vickers hardness, and ΔK_{th} is the threshold stress intensity factor [57].

The calculation process for the critical defect-based fatigue crack growth model in the current study comprises as follows:

(1) Defining the initial crack size using $a = \sqrt{area_{eff}}_{\max}$ for crack depth size and identification of the other dimension of semi-elliptical crack geometry, $2c$, based on surface roughness characterization as depicted in Fig. 4a-b.

When $d_{R-D}$is smaller than the size of the smaller defect ($\sqrt{area_D}$or R_v), then the initial crack depth size is:

$$a = \sqrt{area_D} + R_v + d_{R-D} \tag{3a}$$

Otherwise, the deepest valley of the critical surface profile is considered:

$$a = R_v \tag{3b}$$

Then, the center of the initial semi-elliptic crack is located on the sample's surface at the corresponding critical location around the sample as determined using the introduced approach in Fig. 3, e.g., $\theta = 97^o$ for sample XCT-2. The circumscribed ellipse requires to satisfy the following conditions: the major axis lies at a tangent to the surface, and by definition, the minor axis is shorter than the major axis. This condition leads to determining the other dimension of the semi-elliptical crack, c. It should be noted that the interaction of the surface defects close to each other is also considered in defining the initial semi-elliptical crack geometry. Thus, the initial worst-case crack geometry is determined by considering the interaction of close defects in both dimensions, as shown in Fig. 4b.

(2) The stress intensity factor ΔK is specified for each representative growth point in semi-elliptical crack front using the equations by Newman and Raju [58] employed to the circular cross-section:

$$\Delta K_I = \lambda \Delta\sigma \sqrt{\frac{\pi a}{Q}} f(\phi)$$

$$Q = 1 + 1.464\left(\frac{a}{c}\right)^{1.65}, \lambda = \left[1.13 - 0.09\left(\frac{a}{c}\right)\right]\left[1 + 0.1(1 - \sin\phi)^2\right] f(\phi) = \left[\sin^2\phi + \left(\frac{a}{c}\right)^2 \cos^2\phi\right]^{1/4} \tag{4}$$

where $\Delta\sigma$ is the stress range.

Using this approach, the stress intensity factor of the crack front can be obtained continuously while considering the changes to the crack aspect ratio during fatigue loading.

(3). The representative growth points are moved perpendicular to the semi-elliptic crack front pertain to the Hartman-Schijve variant of NASGRO law [40,59]:

$$\frac{da}{dN} = D\left[\frac{\Delta K - \Delta K_{thr}}{\sqrt{1 - \frac{\Delta K}{(1-R)A}}}\right]^p \tag{5}$$

where D and P are constants, A is the cyclic fracture toughness, and ΔK_{thr} is the threshold stress intensity factor considering mean stress effect named the effective lower fatigue threshold [60]. R is the stress ratio.

It has been demonstrated that the growth of the small cracks can be estimated from Hartman-Schijve long crack representation [60], i.e., Eq. (5), by setting the threshold term to a small value, typically of the order of 0.1 MPa$\sqrt{\text{m}}$. Thus, the small crack growth version of Eq. (5) conforms to the equation:

$$\frac{da}{dN} = D\left[\frac{\Delta K - 0.1}{\sqrt{1 - \frac{\Delta K}{(1-R)A}}}\right]^p \tag{6}$$

D, P are $1.49 \times 10^{-10}, 1.99$, and A is $69MPa\sqrt{m}$ [60].

(4). The obtained growth points are fitted to a semi-ellipse demonstrating the new crack front.

This procedure (Steps 2 through 4) is iterated until the maximum

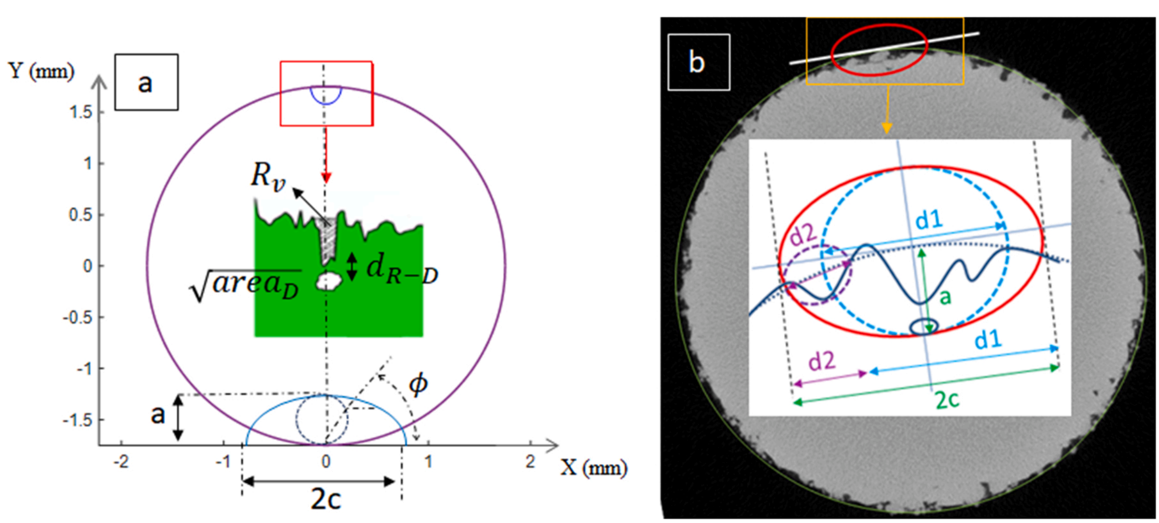

Fig. 4. (a) Schematic diagram of the geometrical parameters defining the surface semi-ellipse crack, and (b) schematic diagram of determining the initial worst-case crack geometry based on the interaction of close defects in both dimensions as applied for the sample XCT-2 for the XCT image at the critical location $Z_v = 6,047mm$.

stress intensity factor for the crack front ($K_{I,\max}$) attain the critical value (K_{IC}) [60], determining the crack growth life of the specimen. Fig. 5a depicts the abovementioned steps for the evolution of the crack size in a flowchart. Fig. 5b shows the implementation of this process schematically. Arrows in this figure demonstrate the perpendicular movement of representative growth points on the semi-elliptic crack front under fatigue loading using the Hartman-Schijve variant of NASGRO law.

4. Results and discussion

4.1. Defects characterization and damage process

In this study, as a first step, distributions of internal defect characteristics (volume, diameter, sphericity, and distance from the edge) have been compared at different stages of the fatigue testing. Fig. 6a-f shows the 3D rendering of internal pores and sum of the pores' volume size distribution along the specimen axis for sample 2-XCT. Defects are not distributed uniformly along the sample's height, and they are mainly distributed on the upper side along the build direction. Nafar Dastgerdi et al. [27] recently demonstrated that the build orientation and layer thickness influence the pores' distribution and volume size, respectively. For the vertically fabricated sample, due to a faster solidification and relatively smaller total melt pool at the upper side, pores have concentrated on the upper side. The average pores density value, i.e., No. of pores/mm^2, is 0.317 for the intact sample. It is worth mentioning that this value for the upper side is 0.578, and for the lower side of the sample, it is 0.079. In this figure, it can be seen that the pores' volume varies during fatigue testing. By increasing the number of cycles up to 72,000 cycles, the pores' volume is increased, as it is also detectable qualitatively from the 3D rendering of pores in this figure. However, this trend is not continued to the next stage, as some of the pores with bigger volume sizes cannot be detected at 76,000 cycles, see an example followed by the blue arrows in Fig. 6a-d. Fig. 6e and f again show increasing pore volume; however, some pores with bigger sizes disappear from 87,000 cycles to 95 000 cycles. The physical justification of this phenomenon relates to the synergistic interaction of two defects in the close vicinity during fatigue loading. Some internal defects link up with surface defects during fatigue loading due to the material degradation of the highly stressed region between close internal and surface defects to each other in the fatigue damage process. This interaction and then merging leads to a decrease in pore population, as seen in the 3D rendering of internal pore distribution. For example, in Fig. 6, the black rectangle shows the disappearance of the internal pores during fatigue loading compared to the corresponding red reference rectangle.

Figs. 7a-e and f-i, respectively, depict the comparison of the sum of the volume of defects along the height of the sample around its axis between the intact sample and each fatigue loading stage and between the two successive fatigue loading stages. Fig. 7a shows the pores' volume increasing around the sample axis. While this increase at some specific radial angle is stopped in the next stage, Fig. 7b, and in some cases, the sum of the pores volume decreases, as depicted with the blue arrows in these figures to be compared with the next step. This trend is repeated in the other steps as the pores' volume increases from 76,000 cycles to 87,000 cycles, highlighted, for example, with the green arrows, and then this increase is stopped at 95 000 cycles, as shown with the blue arrows.

Fig. 8a shows the total volume of pores versus the number of cycles at different stages. It can be seen the total volume of internal pores increases at the first step after 62,000 cycles. This increase continues to the next step at 72,000 cycles, although at a lower rate. Then, the total volume of internal pores decreases at 76000 cycles, and this value increases at an almost similar low rate to the next step, 87,000 cycles. Finally, the pores' total volume increases at 95 000 cycles at a high rate. These results raise an important question about the damage mechanism of the sample in the presence of internal and surface defects under cyclic loading. Another essential factor significantly affecting the fatigue performance of metal AM samples is the distance of pores from the surface of the specimen. Thus, the variation of total pores volume versus the edge distance is investigated at these stages, as shown in the red rectangle in Fig. 8a. In these figures, zero represents the exterior surface, and the edge distance illustrates the radial distance from the external surface to the central axis of the sample. It can be seen with increasing the number of cycles from 62,000–87,000 cycles, that the volume of pores close to the edge is increased, and the possibility of interacting and merging the internal defect with the surface defect is enhanced. The extreme value probability distribution of pores' edge distances is depicted in Fig. 8b to indicate the concentration of the pores close to the surface profiles at different stages compared to the intact state.

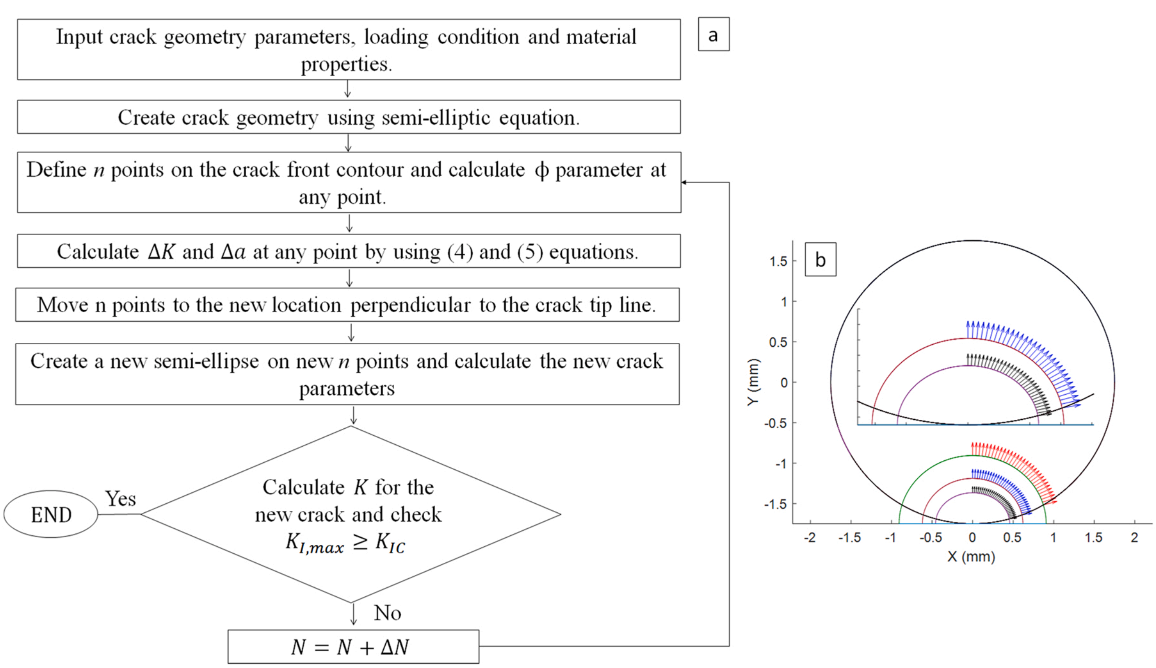

Fig. 5. (a) The process of the evolution of the crack size using the proposed approach, and (b) Schematic diagram of the implementation of the crack growth model.

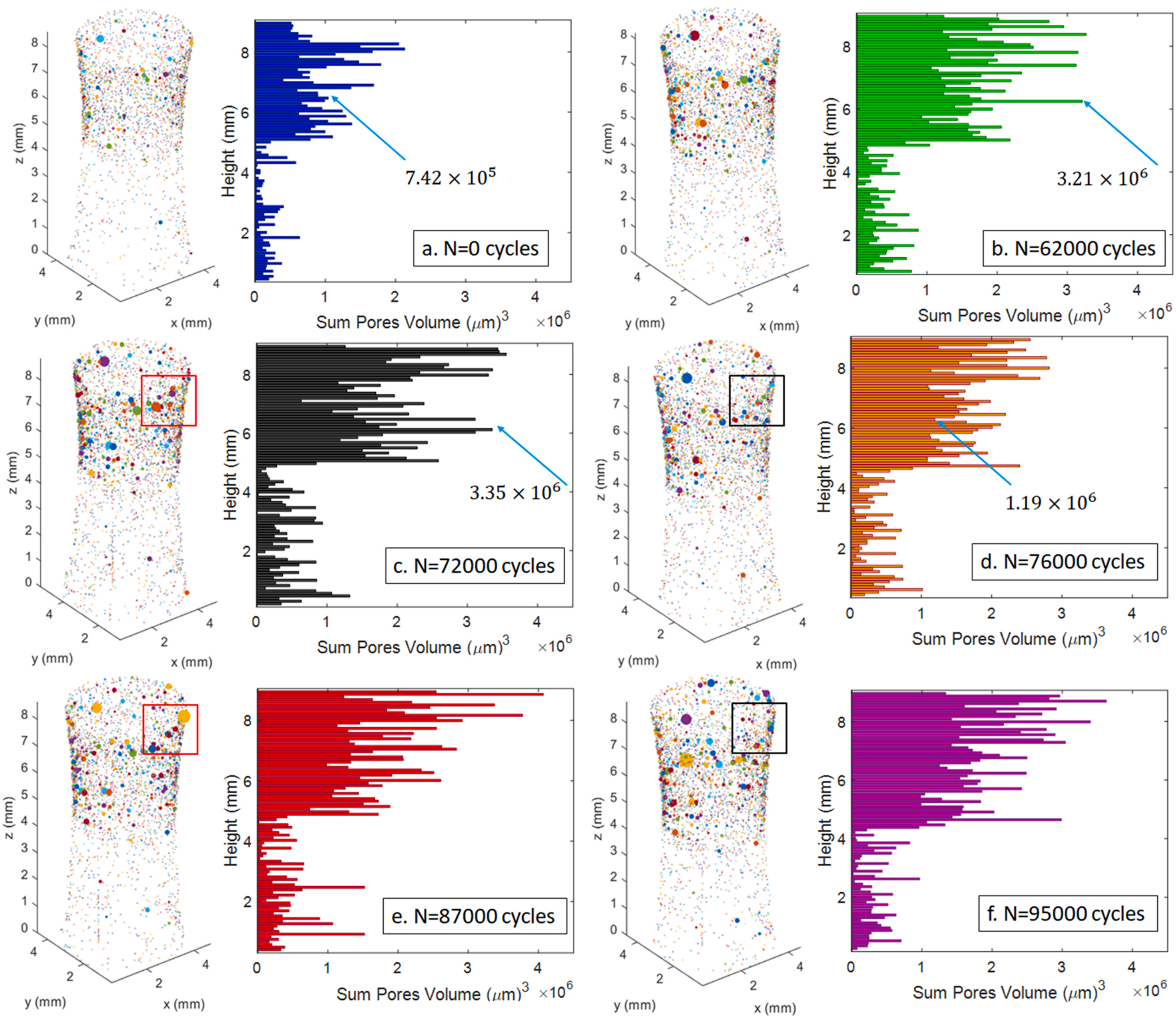

Fig. 6. 3D rendering of internal defects, and pores' volume size distribution along the sample axis at different fatigue loading stages for sample 2-XCT.

Fig. 9 shows an example of interacting and merging the pore close to the edge with surface defect during fatigue testing. This figure provides further evidence and explanation about the results presented in Fig. 6, showing changes in pore volumes and distributions with the increasing number of cycles. Fig. 10 also demonstrates the evidence of the interaction of the surface and internal defects under cyclic loading with some blunted areas connected to the surface from which fatigue cracks tend to initiate and then propagate, as featured in the top views of the fracture surface. Qian et al. [22] and Wu et al. [61,62] have also suggested a phenomenon of linking the internal defects with fatigue cracks initiated from the surface during crack.

propagation. Surface and internal defects induce the local stress concentration. When the distance between the surface and internal defects is very close, the interaction between the stress-concentrated areas close to the surface defects and pores leads to linking surface defects to the pores during fatigue testing. These findings confirm that the effective defect size must be assessed by summing the sizes of internal and surface defects plus the space between two defects, considering the interaction of defects as introduced in Eq. (1).

The extreme value probability distribution of equivalent internal defects' diameter and internal defects' sphericity of the sample at different fatigue steps are depicted in Fig. 11a-b, respectively. Using the extreme value distribution, maximum values in a data set can be determined. Fig. 11a shows the equivalent pores' diameter has increased during fatigue loading. Fig. 11b depicts the probability of pores with lower sphericity have increased under cyclic loading compared to the intact sample. This figure shows the probability of pores with lower sphericity in the lower bound of the data set varies at different fatigue stages. However, the probability distribution is mostly similar for higher sphericity. Sphericity represents the internal defects' morphology. Low sphericity demonstrates irregularity in the defect shape. This finding indicates merging very close pores in the same vicinity into bigger ones with an irregular shape during fatigue testing, although with a small probability. These merged pores with lower sphericity probably work as deleterious defects, lessening the mechanical performance of the sample. It is worth mentioning the same analyses are carried out for sample 1-XCT. Similar trends and results are found for sample 1-XCT.

4.2. Critical equivalent defect size and damage detection

Using the proposed characterization approach to determine $\sqrt{area_{eff}}$, a prediction of fatigue crack initiation is performed for Sample 2-XCT in

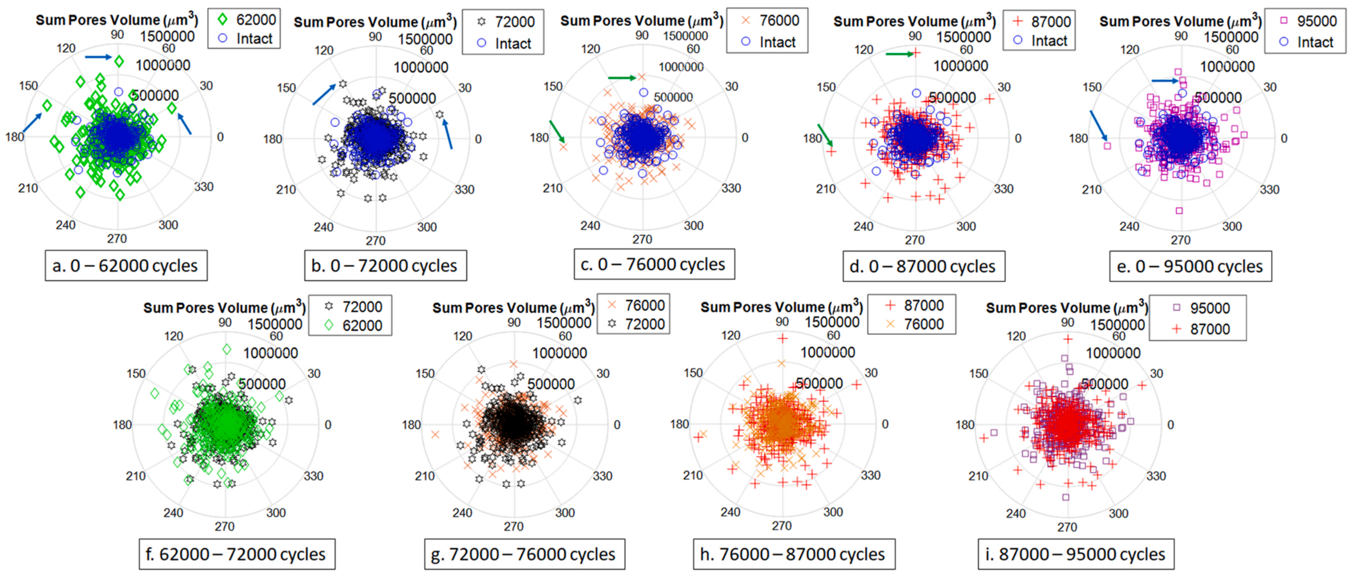

Fig. 7. Comparison of the total volume of pores with respect to the height of the specimen around its axis, (a)-(e) between intact sample and other fatigue loading stages, and (f)-(i) between each two successive fatigue loading stages for sample 2-XCT.

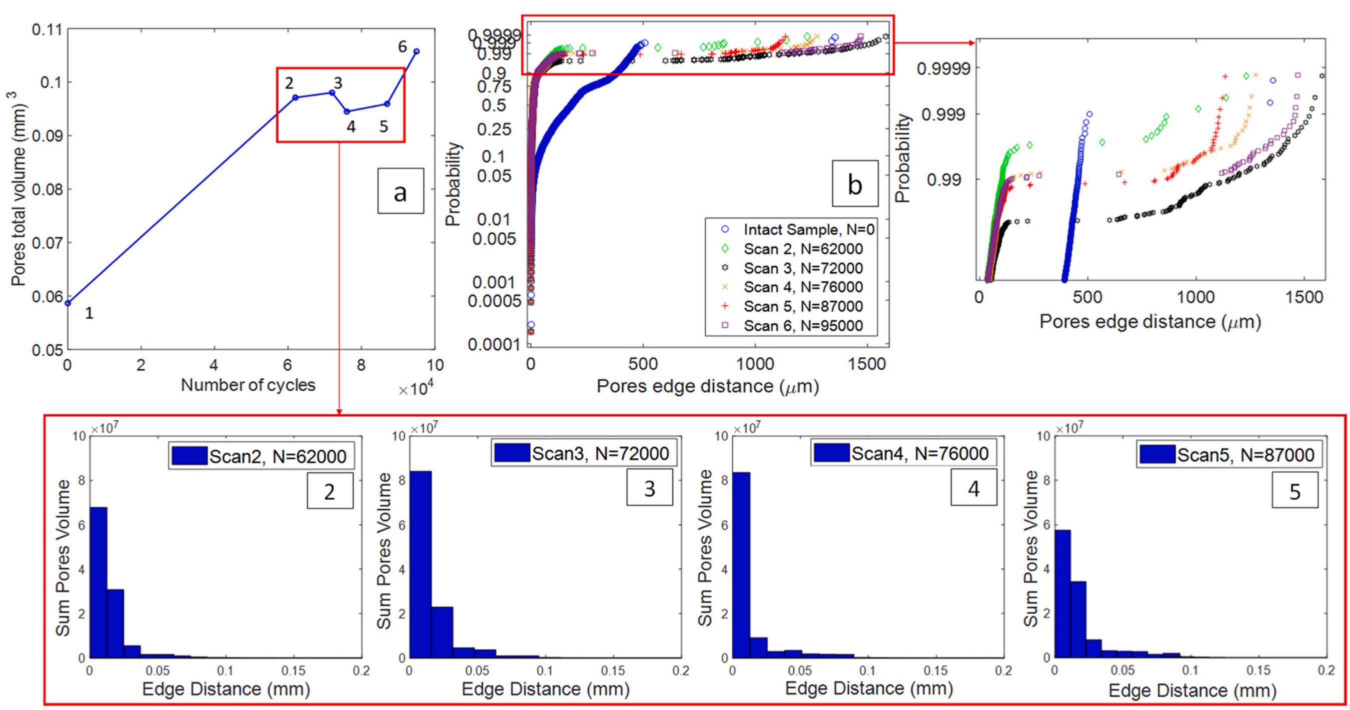

Fig. 8. (a) Variation of the pores total volume and pores' edge distance distribution (b) probability of the pores edge distance at different fatigue steps for sample 2-XCT.

Table 2 and Fig. 12. Table 2 demonstrates the value and location of the critical equivalent defects before testing, and Fig. 12 visualizes these locations for the intact sample and after 95 000 cycles using XCT images.

The predicted locations for fatigue crack initiation are in good agreement with those detected using XCT imaging. The maximum fatigue damage is observed at the predicted critical location ($\theta = 97^o, Z = 6.047mm$) with maximum equivalent defect size. Fig. 13 shows the damage/crack progression path at this location. This figure depicts the crack initiates from the surface and then propagates with a regular elliptical crack front. This figure also shows that the proposed post processing approach applied to the XCT data following the variation of surface profiles can precisely detect the fatigue damage/crack propagation quantitatively and qualitatively, as depicted in Fig. 13a-b.

To highlight the potential of the new damage/crack detection approach for characterizing and 3D rendering of fatigue cracks, the sample's front, surface, and top views after 95 000 cycles are shown in Fig. 14a-d. It is worth mentioning this figure is based on the results of the in-house generated code using the new proposed approach following the variation of surface profiles applied to the XCT imaging and not using the commercial software. This in-house generated code provides the further possibility to characterize and plausibly visualize the fatigue cracks leading to fracture at different locations on the surface, see Fig. 14b, and inside the sample, see Fig. 14d. 3D rendering and the sample's front view in Fig. 14d demonstrate a comparatively flat crack

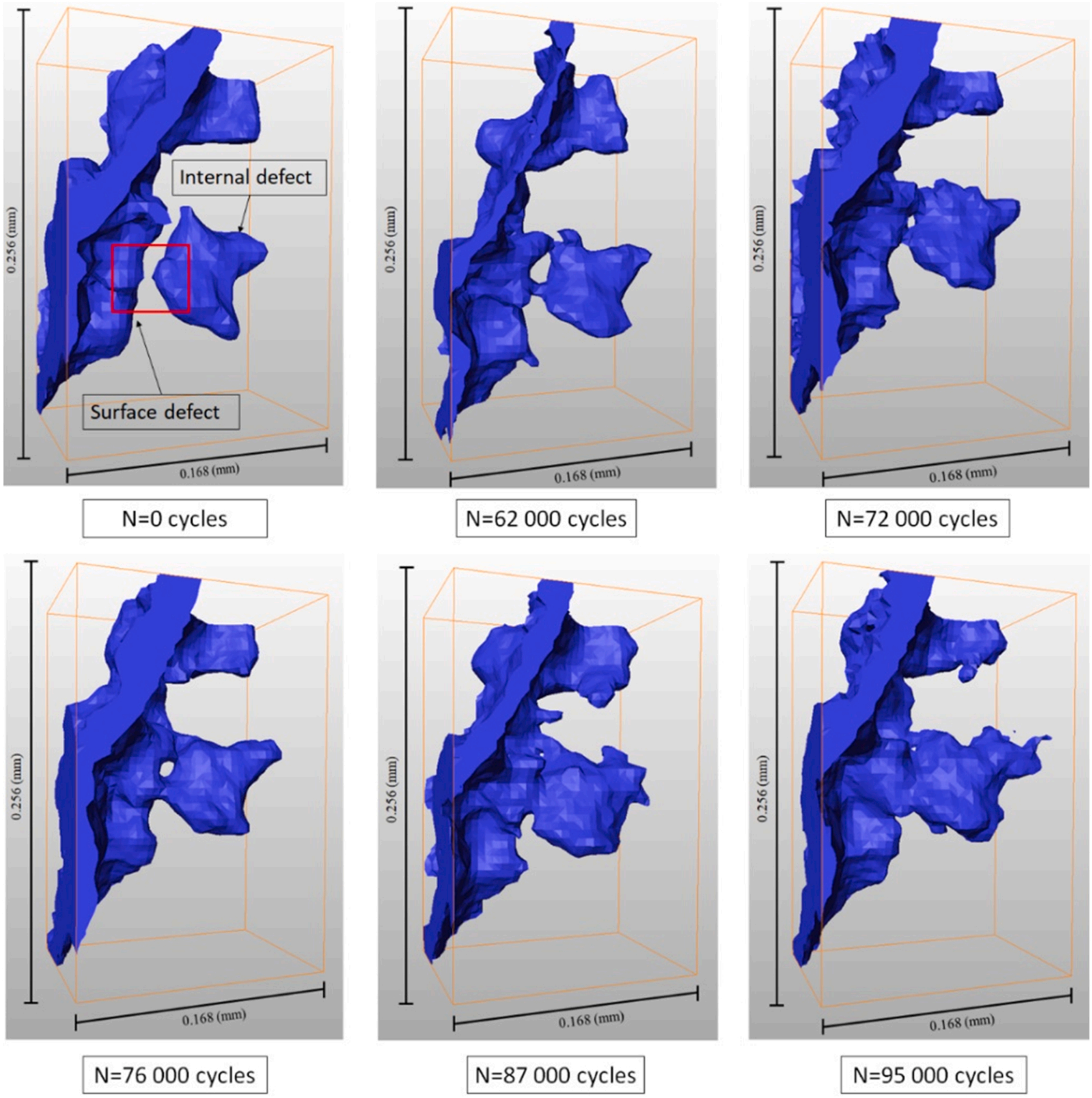

Fig. 9. The merging internal defect with the surface defect for sample 2-XCT during fatigue testing.

growth path of the fatigue cracks at different locations. Being in agreement with the prediction, there are several locations for fatigue crack initiation around the specimen at different heights (see Table 2). The sample's top view in Fig. 14c shows the detected fatigue cracks at different height intervals along the mid-length of the sample. The varying colors represent different height intervals with five intervals 370 μm in length considered. It can be seen all fatigue cracks have an elliptic crack front, and most of the cracks, except the most critical one, have predominantly extended along the surface of the sample.

This study provides novel insight into the initiation and propagation of fatigue cracks for as-built AM parts, considering the effects of internal and surface defects and their interaction. However, other investigations mainly machined the surface of studied samples to remove the surface defect and only focused on the evolution of fatigue damage due to the internal defects or pores [21,22]. In Ref. [22], they only performed XCT at two stages for the intact sample and after 300,000 cycles. This study for the first time provides a practical method to characterize fatigue crack initiation and propagation started from the surface defects at different stages of the fatigue testing. Based on 3D rendering of the cracks front from the XCT imaging, it can be observed that the crack formed at the most critical effective defect in $\theta = 97^o, Z = 6.047mm$ is the dominant one, and the single crack growth model considering the evolution of the crack aspect ratio can be employed for fatigue life prediction.

4.3. Critical defect-based crack growth

In general, it is demonstrated that an individual defect increases the local stress, leading to initiating a short fatigue crack under cyclic loading [63]. Crack propagation transpires when the short fatigue crack can overcome the material barriers in front of the critical defect. Thus, the stress intensity factor of the short crack on the crack front should be analyzed to check the critical values of the crack's front in the depth direction, K_{Ia}, and the crack's edge on the surface, K_{Ic}. The normalized stress intensity factor ratio, K_{Ia}/K_{Ic}, is defined here for further analysis. Fig. 15a shows a sensitivity to the defect's initial defect size and aspect ratio on the stress intensity factor of the semi-elliptical crack at the contour of crack's front related to three predicted defects. One of these defects is the most critical, crack III, and the other two are located close to the most critical one, crack I and II, as schematically depicted in Fig. 15b. It can be observed the variation of K_I along the crack front contour is higher for crack, with a lower aspect ratio and larger initial

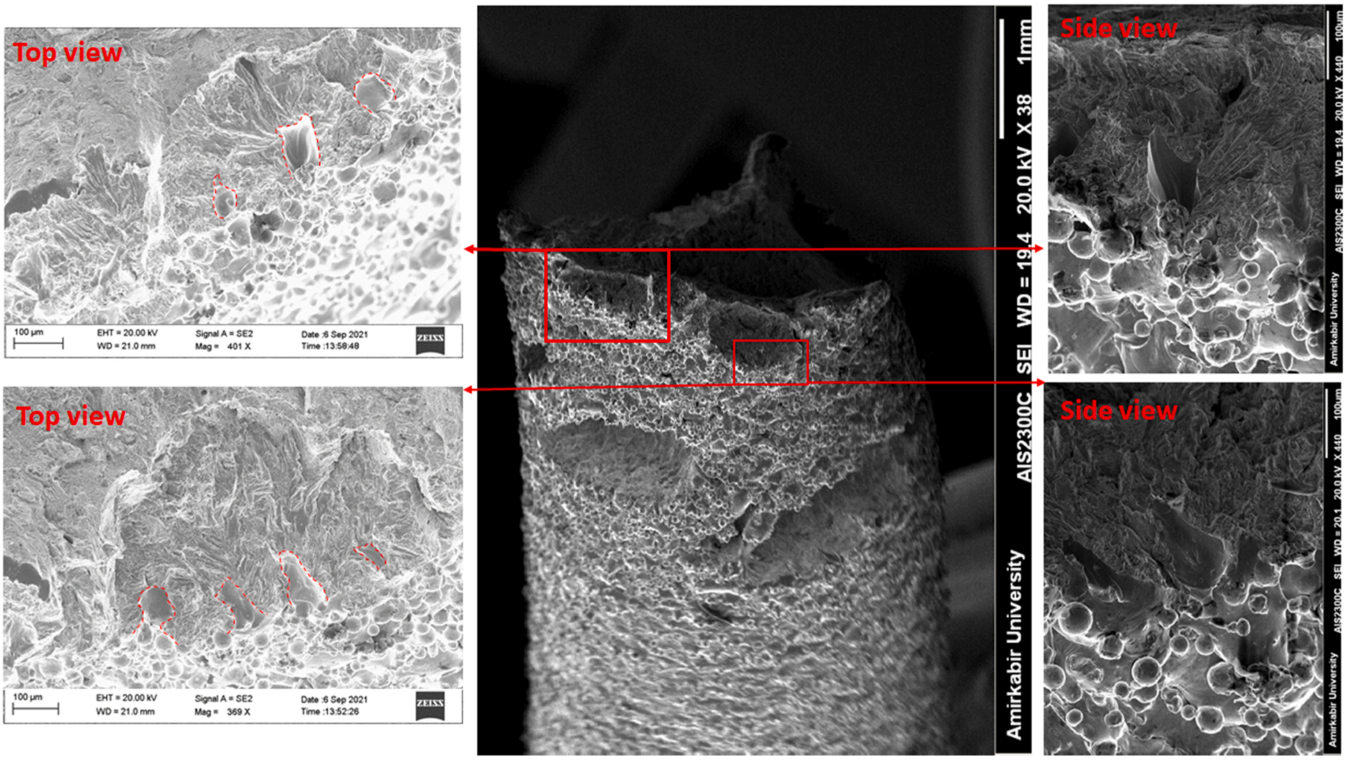

Fig. 10. Top and front view of the damage locations on the fractured surface of the sample 2-XCT showing the interaction of the surface and internal defects featured with the dashed line regions.

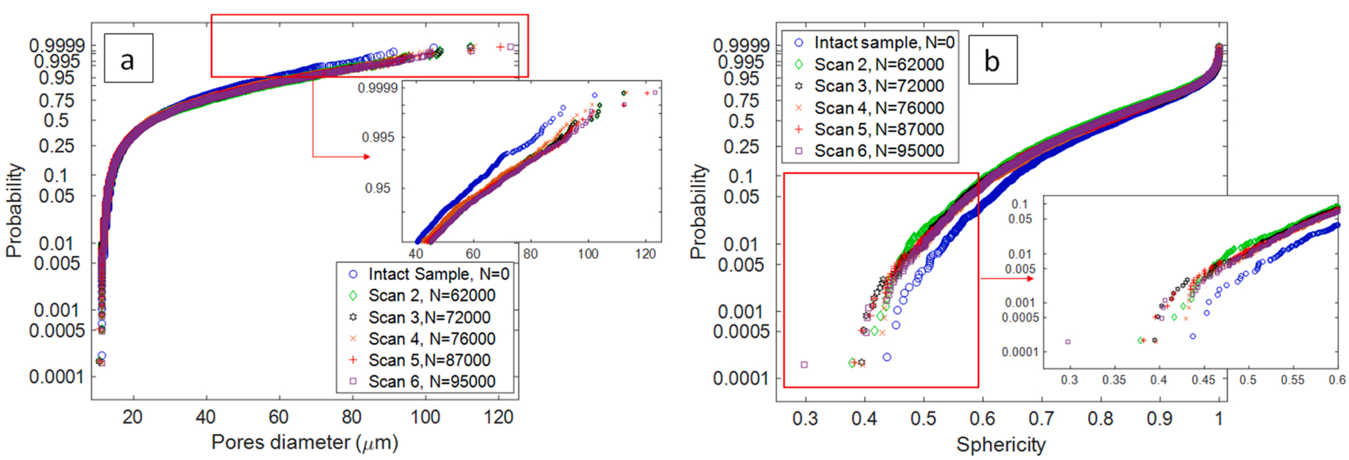

Fig. 11. Comparisons of the (a) equivalent internal defects' diameter, and (b) internal defects' sphericity of sample 2-XCT at different fatigue steps using extreme value probability plots.

crack depth size, as the most critical effective defect. K_{Ia}/K_{Ic} values for different cracks before fatigue testing and after 95 000 loading cycles have been depicted in this figure. Crack III has the highest value, bigger than 1 at both stages compared to cracks I and II. However, the normalized ratio is decreased at the stage of 95 000 loading cycles. It can be seen the stress intensity factor of cracks' edge on the surface has increased after 95 000 loading cycles, especially for cracks I and II. Thus, these cracks tend to extend further on the surface. The superposition of the extent of the fatigue crack after 95 000 cycles onto the fractured surface has been depicted with a blue-tinted area. Based on this finding, it is expected with increasing the loading cycles from 95 000 cycles to the final fracture at 104,003 cycles, crack III still extends in depth ($\frac{K_{Ia}}{K_{Ic}} = 1.085$) and then merges with cracks I and II on the sample's surface. These results also provide a further explanation for Fig. 14c at 95 000 loading cycles, as most of the cracks except the most critical one have extended along the width of the semi-ellipse on the sample's surface. Thus, there is a considerable sensitivity to the defect's initial size and aspect ratio on the defect-based fatigue life prediction of AM parts using fracture mechanics-based approaches, as also reported in Refs. [41,64]. Fig. 15 c shows the predicted extent of the fatigue crack using the proposed critical single crack growth model applied for each crack at different locations. It can be observed there is a good agreement between Fig. 15c and those presented results in Fig. 15 d, which are the superposition of the extent of the fatigue crack after 95,000 cycles (from XCT) onto the fracture surface with blue tints at three different predicted critical locations. In addition, the surface length and depth of semi-elliptical XCT imaging of each crack are also demonstrated in Fig. 15 d.

Table 2
The predicted critical equivalent defect size at the specific height of the sample related to the deepest valleys on critical surface profiles around the sample axis for sample 2-XCT.

θ(deg)	Height(z)(mm)	$\sqrt{area_{eff}}$(μm)
11	5.015	115.375
41	5.536	106.478
87	4.614	109.584
97	6.047	129.246 (Maximum value)
143	5.651	111.011
165	4.939	113.587
217	4.393	125.408
269	5.301	108.841
289	4.559	120.939
296	4.423	80.791
327	4.544	78.250
333	4.544	65.282

Fig. 16a-c shows the front view of the lower part of the broken sample 2-XCT and higher magnification images of critical sites on the surface of the specimen in which damage was initiated. It can be seen there is one main crack propagated on the surface, which means the c dimension increased more than the a (crack depth) for a surface semi-elliptic crack during the crack growth, see Fig. 4. In the higher magnification of the critical site in Fig. 16b, it can be seen there is a sharp notch-like on the surface. The propagation of the fatigue crack is magnified in Fig. 16b$_2$. The higher magnification of the other location in Fig. 16c depicts the example of an internal defect close to the surface. A crack is initiated from this defect toward the surface. Figures 16b$_1$ and 16c$_1$ show the unmelted powders on the surface, which increase the roughness of the surface.

As reported in Table 2, there are several potential sites for fatigue damage initiation, albeit the most critical one with maximum effective defect size value dominantly controls the fatigue damage process. This crack is located in the lower part of the broken sample, where some critical effective defects as initial cracks are predicted. The defect's initial size and aspect ratio result in higher stress intensity factor at the cracks' edge on the surface.

Fig. 17a-c schematically depicts the critical defect-based fatigue crack growth model described in Section 3. First, using the proposed approach in Fig. 3, the initial short crack size has been determined. Then, the crack propagation life is predicted using the single crack model, 51,300 cycles. Fig. 17a shows how the representative growth points progress perpendicularly to the semi-ellipse crack front corresponding to the Hartman-Schijve variant of NASGRO law and the introduced approach in Steps 2 and 3 in Section 3. Since the crack initiation life cannot be determined as assumed the nucleation life to be zero and the short crack growth is predominant for defect-based life analysis [40], the fatigue crack's growth sequence is derived backward in time to validate the introduced fatigue crack growth model. By deriving backward from 104,003 cycles, the sample's total fatigue life, to the 95 000 cycles and comparing Fig. 17b and c, it can be seen the predicted extent of the fatigue crack using the proposed critical single crack growth model and the XCT imaging are in good agreement. The increment of 500 loading cycles is considered for the crack growth in these two figures to reduce the number of iterations in the computation. In the blue area (corresponding to the crack front at 95 000 cycles), the smallest arc and the yellow area is the initial crack determined by the proposed defect's characterization approach, resulting in finding the most critical effective defect with maximum size value. By deriving backward from the sample's total fatigue life (104,003 cycles) and deducting the predicted crack propagation life (51,300 cycles), this point refers to 52,703 cycles of loading, as shown in Fig. 17c. Thus, the crack propagation life anticipated using the model accounts for around 49% of the total fatigue lifetime, and the initiation stage accounts for 51% of the total life. This result is in good correlation with our findings from the XCT measurements for sample 2-XCT that the initiation step was 60% of the total life. Thus, a considerable fraction of the fatigue life is consumed in the initiation of small cracks, as also reported in Ref. [21] that for AM-processed Ti alloy, the initiation stage made up a significant fraction of the total life, around 70%. The results indicate that the crack growth behavior of the single crack initiation case is well demonstrated using the introduced approach.

The proposed critical defect-based fatigue crack growth model predicts the crack's propagation life. Thus, the sample's total fatigue life, $N_{f,model}$, can be determined by considering the initiation life of the short crack,$N_{initiation}$, as 60%– 65% of the total life and summing with the fatigue propagation life, $N_{p,model}$. It should be noted that the crack initiation step in the percentage of the total life is sensitive to the studied domain, and thus 60%– 65% of the total life is only valid in the high cycle domain of 10^6 cycles. The comparison of the predicted and experimental fatigue lives of the tested specimens in this work is presented in Table 3. In this table, the weight selection for $N_{initiation}$ has been considered based on the experimental findings from the ex-situ fatigue teste for each sample. It can be observed there is a good agreement between the predicted and experimental values.

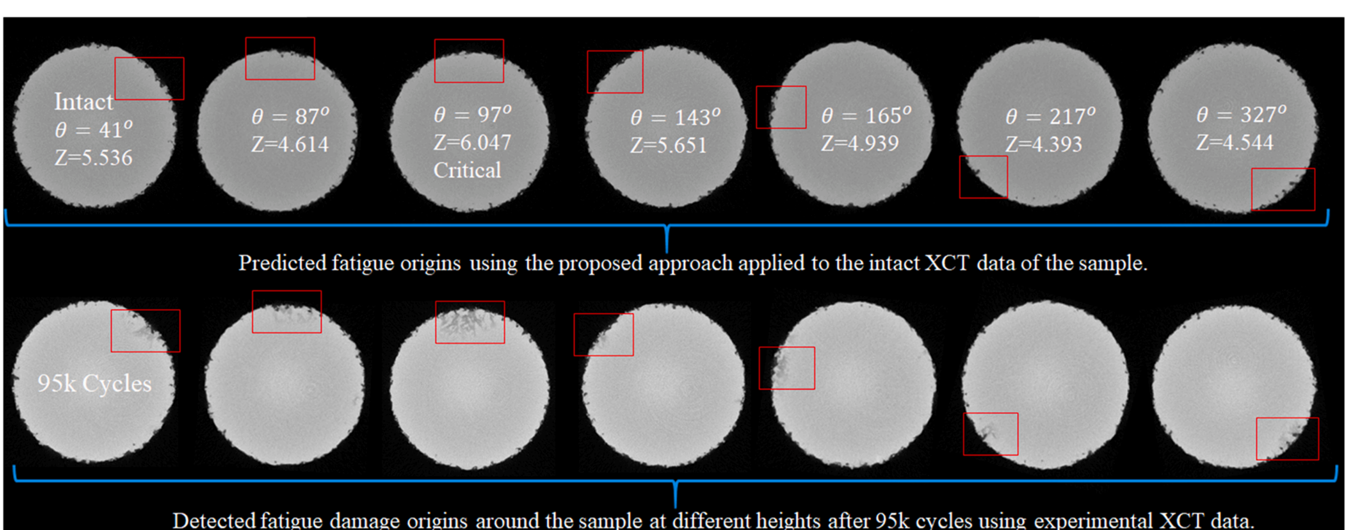

Fig. 12. Comparison of the exemplary of predicted fatigue origins before testing and detected fatigue damage origins after 95 000 cycles for sample 2-XCT. The images are for locations in different radial angles and heights along the sample axis from left to right.

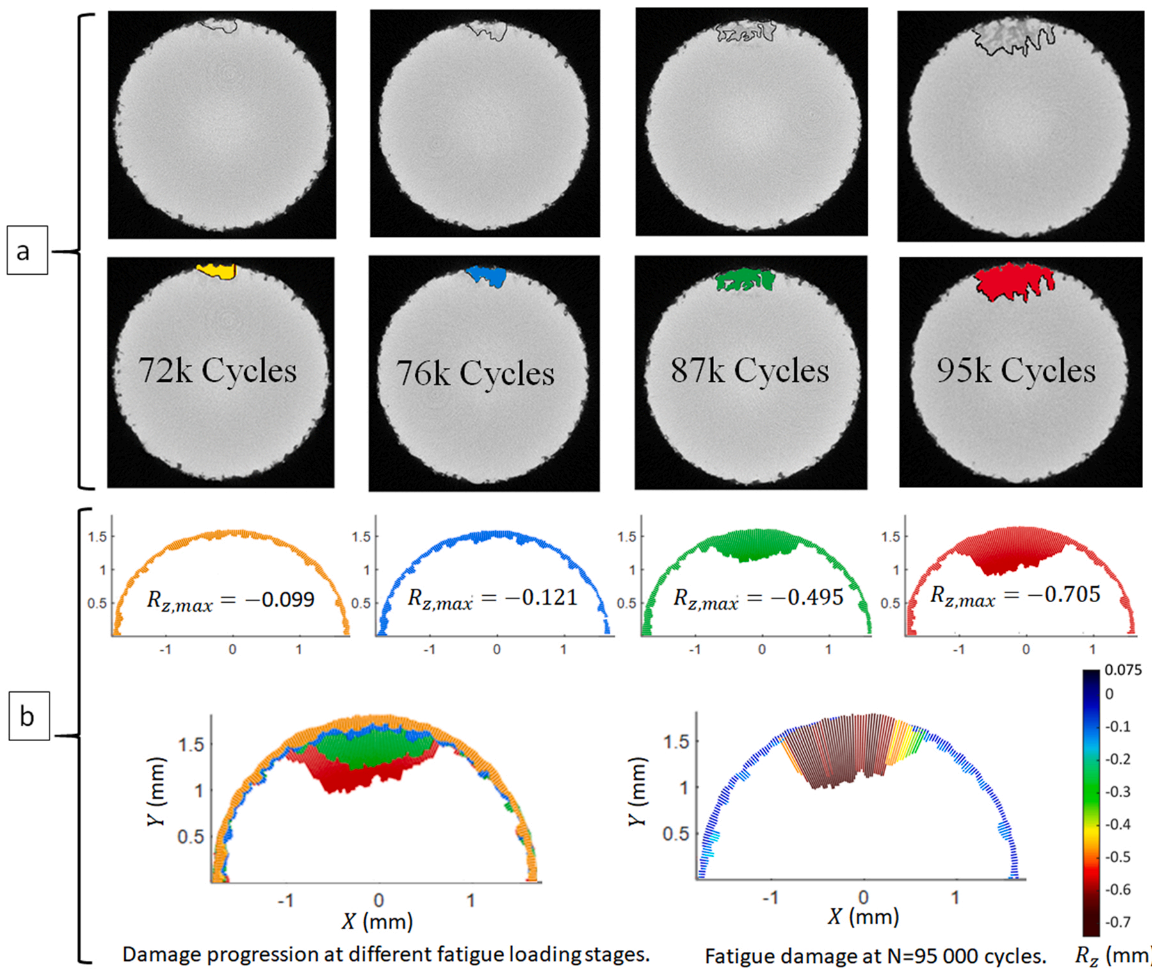

Fig. 13. Fatigue damage evolution in sample 2-XCT at different fatigue loading stages for the predicted critical location ($\theta = 97^o, Z = 6.047mm$), (a) qualitatively detected from XCT images, (b) quantitatively detected using the damage detection algorithm based on the post-processing of the XCT data.

4.4. Fracture surface analysis

To better elucidate the failure mechanism, the fracture surface of the tested sample 2-XCT is examined by scanning electron microscopy (SEM), as depicted in Fig. 18. It can be seen fatigue origins have been located at many locations around the sample axis at different heights, as predicted in Table 1 before fatigue testing. The failure mode implies the initiation of multiple cracks. These multiple cracks coalesce during crack propagation, as confirmed by ledges [65] (marked by yellow signs in Fig. 18) on the fracture surface, speeding up fatigue failure. When two cracks are located slightly off the same plane and during their growth start to overlap, a fracture of the bridging ligament would happen, leading to ridges on the fracture surfaces, as confirmed by numbers of ledges on the fracture surface. Thus, the fracture surfaces merging to create the final crack are not all placed on a single plane. Based on the XCT acquired data and characterization of the multiple cracks around the sample at different heights, as depicted in Fig. 14 after 95 000 fatigue cycles, it can be observed multiple fatigue cracks propagate in different planes. Thus, the coalescence, as evidenced on the fractured surface, occurs at the final 10% of the total fatigue life, between 95 000 and 104,003 cycles. This finding also confirms the single crack model with an appropriate characterization approach to detect the critical initial defect size as a short crack can be a practical approach for fatigue life prediction of metal AM parts. However, it may result in a non-conservative assessment since it cannot precisely consider the real multiple crack propagation phenomena, as a discrepancy between experiments and the model prediction results is reported in Table 3. Recently, Qian et al. [22] presented a multiple crack growth model for additively manufactured AlSi10Mg alloy based on the proposed approach in Refs. [66,67] with the assumption that all fatigue cracks merging to create the final fractured surface have been placed on the same plane. This multiple fatigue crack growth model predicts that the coalescence process of multiple cracks at the fractured surface occurs between 50% and 60% of the total fatigue life of the samples. As mentioned, they only scanned the sample at two stages, before fatigue testing, and after 300,000 fatigue cycles. Thus, it is challenging to clarify the role of multiple defects in crack initiation, their coalescence, and progress under fatigue loading. However, this study provides further insight into the fatigue damage process of AM stainless steels during fatigue testing using XCT imaging at different stages. Further study is still required to propose a synergistic multiple- fatigue crack growth model in predicting the total fatigue life based on actual phenomena, as planned for future work.

5. Conclusion

This paper employed XCT imaging during fatigue testing to provide further information on the fatigue behavior of AM stainless steel 316 L parts. Moreover, an analytical framework has been introduced for defect-based fatigue life prediction of AM metals using the equivalent defect size parameter, $\sqrt{area_{eff}}$, and the Hartman-Schijve variant of NASGRO equations were utilized to consider the progression of the crack aspect ratio during its growth. Significant contributions of this study can be summarized as follows:

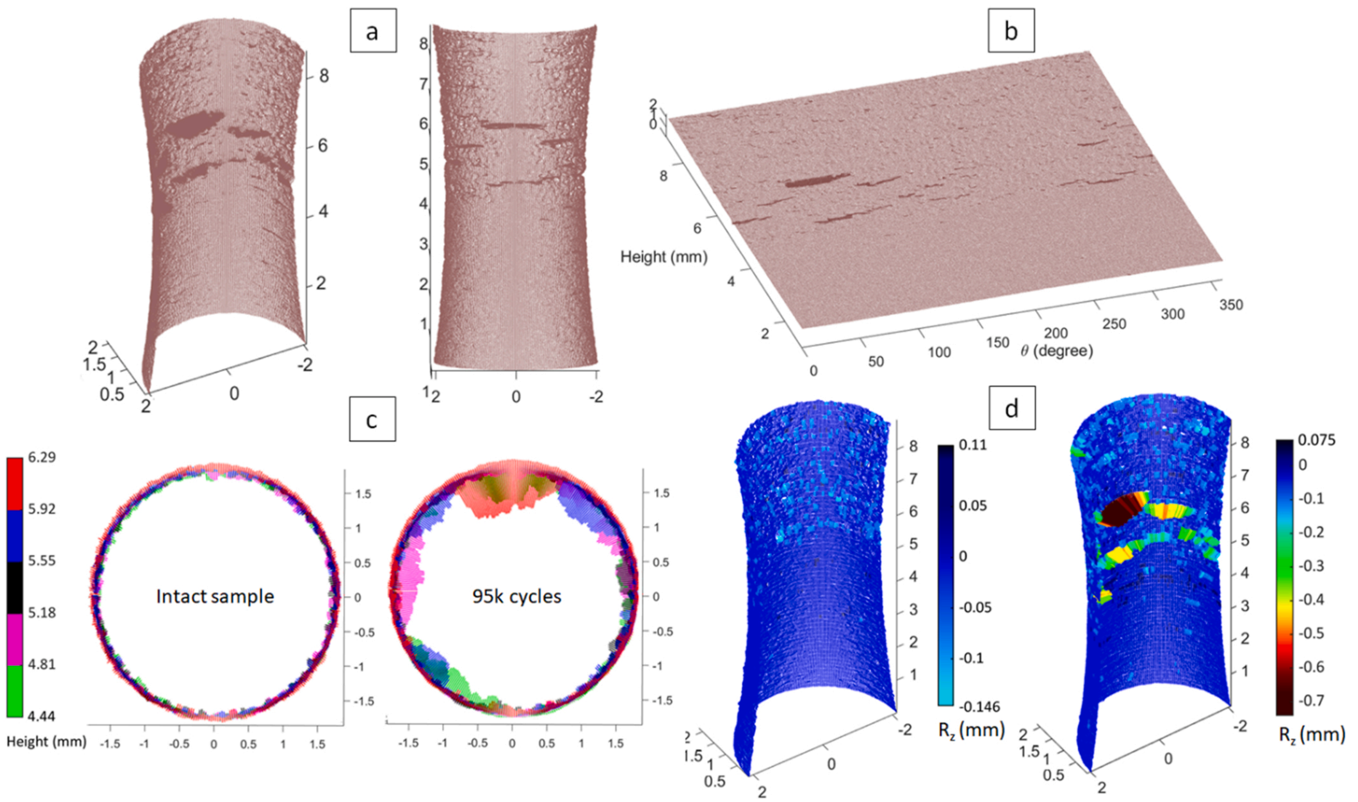

Fig. 14. (a) Rendered front and (b) surface view of sample 2-XCT at N = 95 000 cycles, and (c) top and (d) front view of the sample at N = 0 and N = 95 000 cycles using the damage detection algorithm based on the post-processing of the XCT data for detecting the surface profiles and calculating the surface roughness.

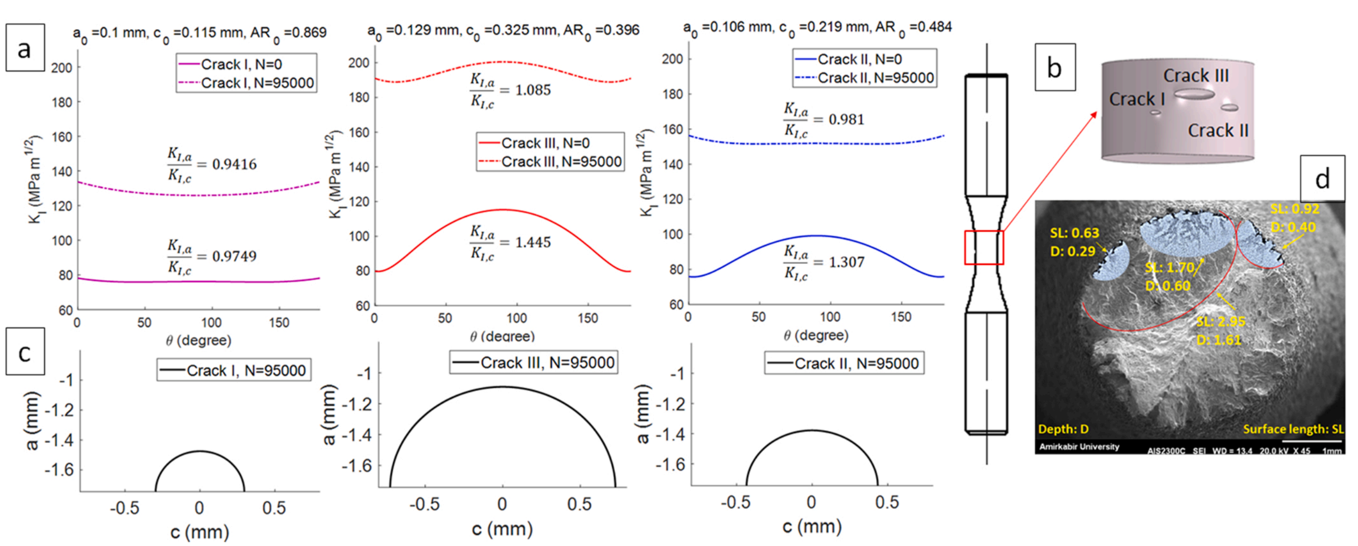

Fig. 15. (a) Variation of the stress intensity factor at the edge contour of the semi elliptical crack for three different initial predicted cracks' size and aspect ratio at (b) different locations around the sample at different heights (schematic view) for intact sample (N = 0) and after 95 000 cycles. (c) The predicted extent of the fatigue crack using the proposed critical single crack growth model applied for each crack at different locations after 95 000 cycles. (d) Superposition of the extent of the fatigue crack after 95 000 cycles (from XCT) onto the fracture surface at three different predicted critical locations (crack I ($\theta = 41^o, Z = 5.536mm$), crack II ($\theta = 143^o, Z = 5.651mm$), crack III ($\theta = 97^o, Z = 6.047mm$)).

- The proposed defect and damage detection algorithm using the post-processing of XCT data following the variation of surface profiles around the sample can precisely detect fatigue crack initiation and follow the fatigue crack propagation at different stages during fatigue testing.
- The ex-situ XCT during the fatigue test provides novel information on fatigue crack formation and the interaction between surface and internal defects. A considerable fraction of the fatigue life is consumed in initiating small cracks (more than 60% of fatigue life). In the later stages of the fatigue life, the possibility of interacting and merging the internal and surface defects increases.
- It is proven that the proposed approach can predict the fatigue crack origin using the equivalent defect size parameter, $\sqrt{area_{eff}}$, based on

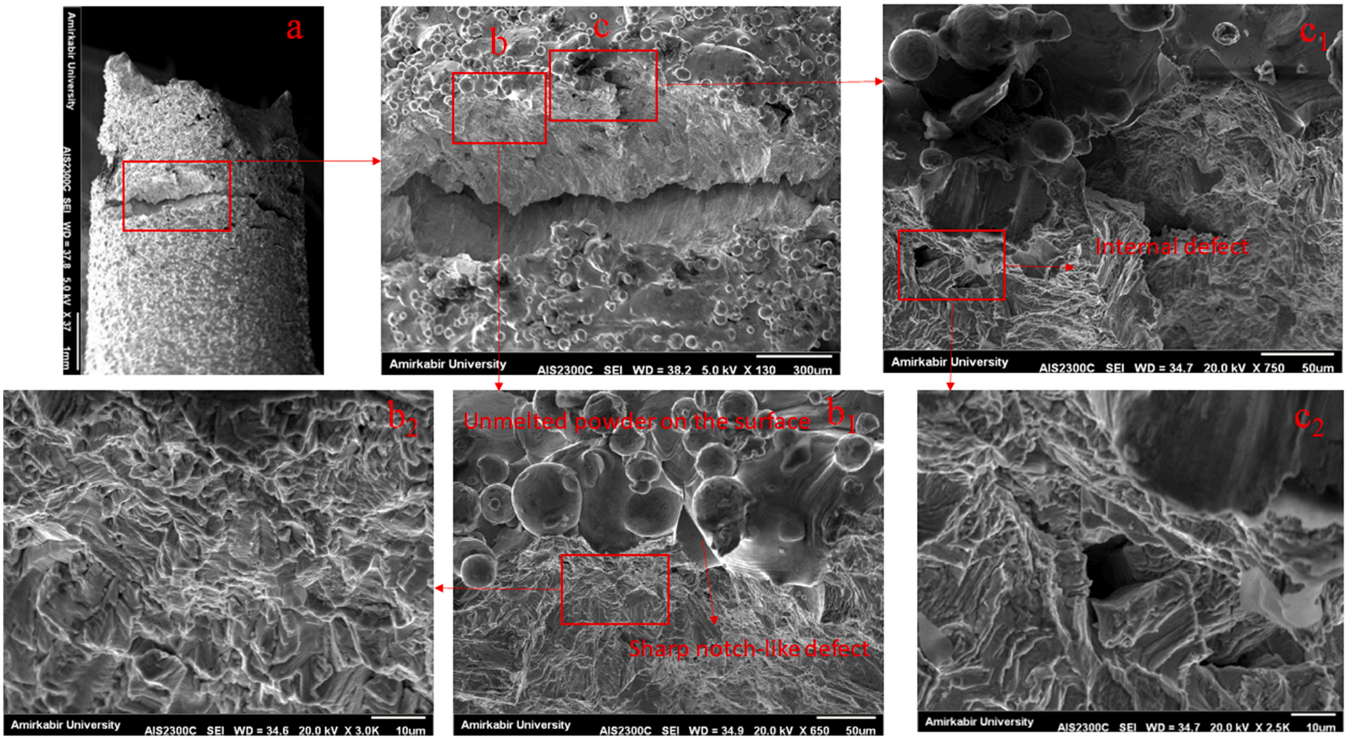

Fig. 16. (a) Front view fractography of the damage location on the lower part of the broken sample 2-XCT, (b), and (c) higher magnification images of critical sites on the surface of the specimen in which damage was initiated.

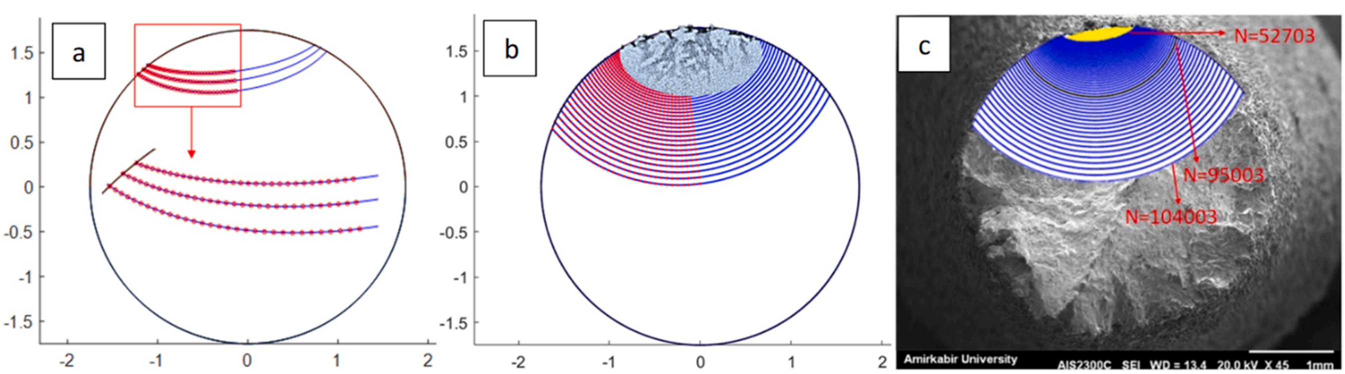

Fig. 17. (a) Schematic diagram of the critical defect-based fatigue crack growth model, (b) superposition of the extent of the fatigue crack after 95 000 cycles (from XCT) onto the modeled crack growth sequence, and (c) superposition of the modeled crack growth step onto the fracture surface of the sample 2-XCT, with the initial crack and the extent of the fatigue crack at final failure shown by yellow and blue tints, respectively.

Table 3
Comparison of the predicted and experimental fatigue life for samples.

Sample	$\sqrt{\mathbf{area_{eff}}}_{max}(\mathbf{\mu m})$	$N_{p,model}$	$N_{initiation}$	$N_{f,model} = N_{p,model} + N_{initiation}$	$N_{f,exp}/N_{f,model}$
1-XCT $\sigma = 170MPa$	155.154	62 400	$0.65N_{f,model}$	178 286	0.74
2-XCT $\sigma = 190MPa$	129.246	51 300	$0.6N_{f,model}$	128 250	0.81

defects' features and the synergistic effects of internal and surface defects.

- The damage/crack progression dominantly occurs at the predicted maximum equivalent defect size, and $\sqrt{area_{eff}}_{\max}$ is found suitable to be considered as an initial small crack size for crack growth simulations.
- The single crack model, which can effectively predict the evolution of the crack front aspect ratio with an appropriate characterization approach to detect the initial worst-case crack geometry, can be a suitable engineering approach for fatigue life prediction of metal AM components in the presence of internal and surface defects.

CRediT authorship contribution statement

Toudeshky Hossein Hosseini: Writing – review & editing, Validation. **Kuva Jukka:** Writing – review & editing, Software, Data curation.

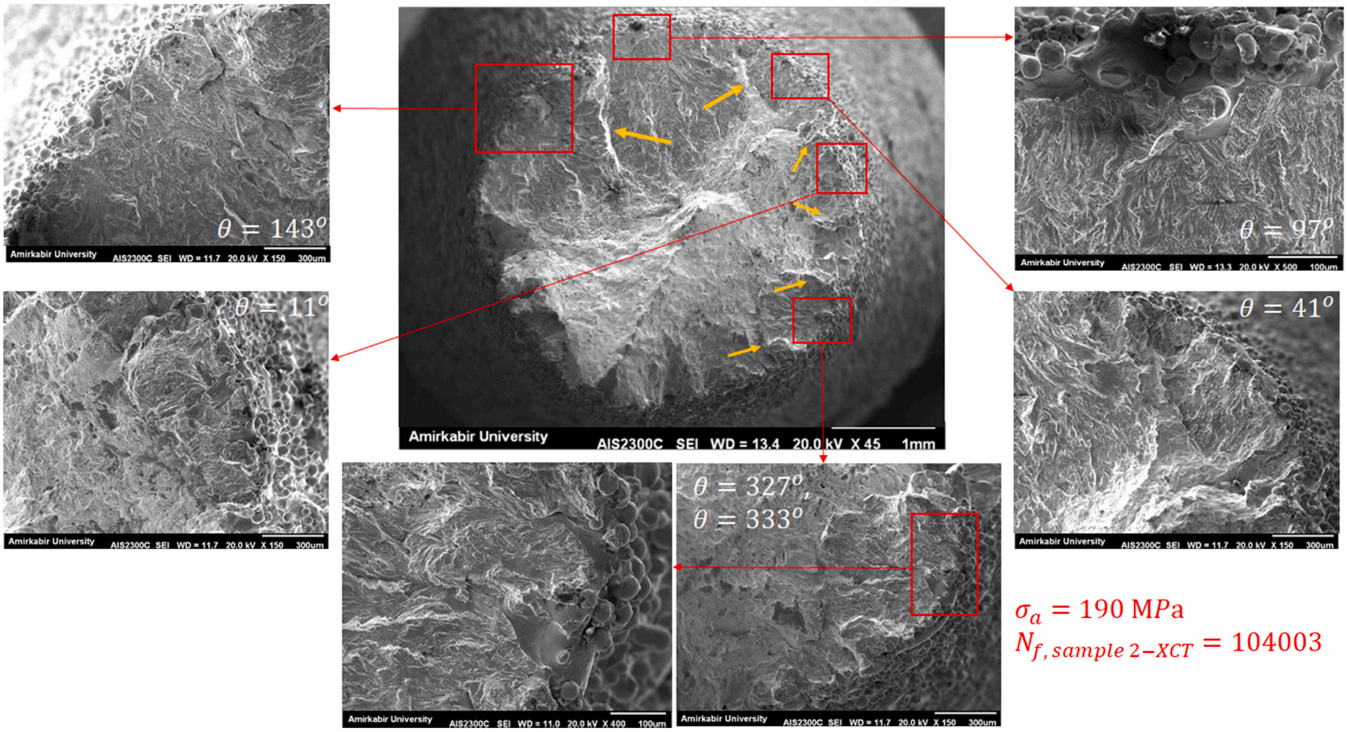

Fig. 18. SEM top views of the fracture surface of the sample 2-XCT that failed due to volumetric defects and surface features located at different planar. Sample tested at stress amplitude of 190 MPa. Higher magnification images showing the crack initiation sites.

Remes Heikki: Writing – review & editing, Validation, Resources, Conceptualization. **Lehto Pauli:** Writing – review & editing, Validation. **Nafar Dastgerdi Jairan:** Writing – original draft, Validation, Supervision, Software, Methodology, Investigation, Formal analysis, Data curation, Conceptualization. **Jaberi Omid:** Visualization, Software, Methodology, Formal analysis.

Declaration of Competing Interest

The authors declare that they have no known competing financial interests or personal relationships that could have appeared to influence the work reported in this paper.

Data Availability

Data will be made available on request.

Acknowledgement

This research was supported by the Solid Mechanics Laboratory of Aalto University.

References

[1] S. Cooke, K. Ahmadi, S. Willerth, R. Herring, Metal additive manufacturing: technology, metallurgy and modelling, J. Manuf. Process 57 (2020) 978–1003, https://doi.org/10.1016/j.jmapro.2020.07.025.

[2] B. Blakey-Milner, P. Gradl, G. Snedden, M. Brooks, J. Pitot, E. Lopez, M. Leary, F. Berto, A. du Plessis, Metal additive manufacturing in aerospace: a review, Mater. Des. 209 (2021), 110008, https://doi.org/10.1016/j.matdes.2021.110008.

[3] F. Khodabakhshi, M.H. Farshidianfar, A.P. Gerlich, M. Nosko, V. Trembošová, A. Khajepour, Effects of laser additive manufacturing on microstructure and crystallographic texture of austenitic and martensitic stainless steels, Addit. Manuf. 31 (2020), 100915, https://doi.org/10.1016/j.addma.2019.100915.

[4] W.E. Frazier, Metal additive manufacturing: a review, J. Mater. Eng. Perform. 23 (2014) 1917–1928, https://doi.org/10.1007/s11665-014-0958-z.

[5] Y. Kok, X.P. Tan, P. Wang, M.L.S. Nai, N.H. Loh, E. Liu, S.B. Tor, Anisotropy and heterogeneity of microstructure and mechanical properties in metal additive manufacturing: a critical review, Mater. Des. 139 (2018) 565–586, https://doi.org/10.1016/j.matdes.2017.11.021.

[6] S. Chen, H. Gao, Y. Zhang, Q. Wu, Z. Gao, X. Zhou, Review on residual stresses in metal additive manufacturing: formation mechanisms, parameter dependencies, prediction and control approaches, J. Mater. Res. Technol. 17 (2022) 2950–2974, https://doi.org/10.1016/j.jmrt.2022.02.054.

[7] N. Sanaei, A. Fatemi, Defects in additive manufactured metals and their effect on fatigue performance: a state-of-the-art review, Prog. Mater. Sci. 117 (2021), 100724, https://doi.org/10.1016/j.pmatsci.2020.100724.

[8] T. Persenot, A. Burr, G. Martin, J.-Y. Buffiere, R. Dendievel, E. Maire, Effect of build orientation on the fatigue properties of as-built electron beam melted Ti-6Al-4V alloy, Int. J. Fatigue 118 (2019) 65–76, https://doi.org/10.1016/j.ijfatigue.2018.08.006.

[9] S. Romano, A. Brückner-Foit, A. Brandão, J. Gumpinger, T. Ghidini, S. Beretta, Fatigue properties of AlSi10Mg obtained by additive manufacturing: defect-based modelling and prediction of fatigue strength, Eng. Fract. Mech. 187 (2018) 165–189, https://doi.org/10.1016/j.engfracmech.2017.11.002.

[10] S. Siddique, M. Imran, F. Walther, Very high cycle fatigue and fatigue crack propagation behavior of selective laser melted AlSi12 alloy, Int. J. Fatigue 94 (2017) 246–254, https://doi.org/10.1016/j.ijfatigue.2016.06.003.

[11] W.J. Sames, F.A. List, S. Pannala, R.R. Dehoff, S.S. Babu, The metallurgy and processing science of metal additive manufacturing, Int. Mater. Rev. 61 (2016) 315–360, https://doi.org/10.1080/09506608.2015.1116649.

[12] N. Haghdadi, M. Laleh, M. Moyle, S. Primig, Additive manufacturing of steels: a review of achievements and challenges, J. Mater. Sci. 56 (2021) 64–107, https://doi.org/10.1007/s10853-020-05109-0.

[13] Z. Quan, Z. Larimore, X. Qin, J. Yu, M. Mirotznik, J.-H. Byun, Y. Oh, T.-W. Chou, Microstructural characterization of additively manufactured multi-directional preforms and composites via X-ray micro-computed tomography, Compos. Sci. Technol. 131 (2016) 48–60, https://doi.org/10.1016/j.compscitech.2016.05.015.

[14] J. Nafar Dastgerdi, A. Miettinen, J. Parkkonen, H. Remes, Multiscale microstructural characterization of particulate-reinforced composite with non-destructive X-ray micro- and nanotomography, Compos. Struct. 194 (2018) 292–301, https://doi.org/10.1016/j.compstruct.2018.04.022.

[15] A. du Plessis, I. Yadroitsava, I. Yadroitsev, Effects of defects on mechanical properties in metal additive manufacturing: a review focusing on X-ray tomography insights, Mater. Des. 187 (2020), 108385, https://doi.org/10.1016/j.matdes.2019.108385.

[16] H. Choo, M.R. Koehler, L.P. White, Y. Ren, D. Morin, E. Garlea, Influence of defect characteristics on tensile deformation of an additively manufactured stainless steel: Evolutions of texture and intergranular strain, Mater. Sci. Eng. A. 791 (2020), 139637, https://doi.org/10.1016/j.msea.2020.139637.

[17] S. Ghods, R. Schur, E. Schultz, R. Pahuja, A. Montelione, C. Wisdom, D. Arola, M. Ramulu, Powder reuse and its contribution to porosity in additive manufacturing of Ti6Al4V, Materialia 15 (2021), 100992, https://doi.org/10.1016/j.mtla.2020.100992.

[18] F.H. Kim, S.P. Moylan, E.J. Garboczi, J.A. Slotwinski, Investigation of pore structure in cobalt chrome additively manufactured parts using X-ray computed tomography and three-dimensional image analysis, Addit. Manuf. 17 (2017) 23–38, https://doi.org/10.1016/j.addma.2017.06.011.
[19] K. Heim, F. Bernier, R. Pelletier, L.-P. Lefebvre, High resolution pore size analysis in metallic powders by X-ray tomography, Case Stud. Nondestruct. Test. Eval. 6 (2016) 45–52, https://doi.org/10.1016/j.csndt.2016.09.002.
[20] S. Romano, A. Brandão, J. Gumpinger, M. Gschweitl, S. Beretta, Qualification of AM parts: extreme value statistics applied to tomographic measurements, Mater. Des. 131 (2017) 32–48, https://doi.org/10.1016/j.matdes.2017.05.091.
[21] S. Tammas-Williams, P.J. Withers, I. Todd, P.B. Prangnell, The influence of porosity on fatigue crack initiation in additively manufactured titanium components, Sci. Rep. 7 (2017) 7308, https://doi.org/10.1038/s41598-017-06504-5.
[22] W. Qian, S. Wu, Z. Wu, S. Ahmed, W. Zhang, G. Qian, P.J. Withers, In situ X-ray imaging of fatigue crack growth from multiple defects in additively manufactured AlSi10Mg alloy, Int. J. Fatigue 155 (2022), 106616, https://doi.org/10.1016/j.ijfatigue.2021.106616.
[23] A. Yadollahi, N. Shamsaei, Additive manufacturing of fatigue resistant materials: challenges and opportunities, Int. J. Fatigue 98 (2017) 14–31, https://doi.org/10.1016/j.ijfatigue.2017.01.001.
[24] M. Hamidi Nasab, S. Romano, D. Gastaldi, S. Beretta, M. Vedani, Combined effect of surface anomalies and volumetric defects on fatigue assessment of AlSi7Mg fabricated via laser powder bed fusion, Addit. Manuf. 34 (2020), 100918, https://doi.org/10.1016/j.addma.2019.100918.
[25] S. Romano, P.D. Nezhadfar, N. Shamsaei, M. Seifi, S. Beretta, High cycle fatigue behavior and life prediction for additively manufactured 17-4 PH stainless steel: effect of sub-surface porosity and surface roughness, Theor. Appl. Fract. Mech. 106 (2020), 102477, https://doi.org/10.1016/j.tafmec.2020.102477.
[26] H.Y. Wan, Y.W. Luo, B. Zhang, Z.M. Song, L.Y. Wang, Z.J. Zhou, C.P. Li, G.F. Chen, G.P. Zhang, Effects of surface roughness and build thickness on fatigue properties of selective laser melted Inconel 718 at 650 °C, Int. J. Fatigue 137 (2020), 105654, https://doi.org/10.1016/j.ijfatigue.2020.105654.
[27] J. Nafar Dastgerdi, O. Jaberi, H. Remes, Influence of internal and surface defects on the fatigue performance of additively manufactured stainless steel 316L, Int. J. Fatigue 163 (2022), 107025, https://doi.org/10.1016/j.ijfatigue.2022.107025.
[28] W. Schneller, M. Leitner, S. Pomberger, F. Grün, S. Leuders, T. Pfeifer, O. Jantschner, Fatigue strength assessment of additively manufactured metallic structures considering bulk and surface layer characteristics, Addit. Manuf. 40 (2021), 101930, https://doi.org/10.1016/j.addma.2021.101930.
[29] A. Townsend, N. Senin, L. Blunt, R.K. Leach, J.S. Taylor, Surface texture metrology for metal additive manufacturing: a review, Precis. Eng. 46 (2016) 34–47, https://doi.org/10.1016/j.precisioneng.2016.06.001.
[30] Y.N. Hu, S.C. Wu, P.J. Withers, J. Zhang, H.Y.X. Bao, Y.N. Fu, G.Z. Kang, The effect of manufacturing defects on the fatigue life of selective laser melted Ti-6Al-4V structures, Mater. Des. 192 (2020), 108708, https://doi.org/10.1016/j.matdes.2020.108708.
[31] H.Y. Wan, Y.W. Luo, B. Zhang, Z.M. Song, L.Y. Wang, Z.J. Zhou, C.P. Li, G.F. Chen, G.P. Zhang, Effects of surface roughness and build thickness on fatigue properties of selective laser melted Inconel 718 at 650 °C, Int. J. Fatigue 137 (2020), 105654, https://doi.org/10.1016/j.ijfatigue.2020.105654.
[32] L. Barricelli, S. Beretta, Analysis of prospective SIF and shielding effect for cylindrical rough surfaces obtained by L-PBF, Eng. Fract. Mech. 256 (2021), 107983, https://doi.org/10.1016/j.engfracmech.2021.107983.
[33] T. Persenot, A. Burr, R. Dendievel, J.-Y. Buffière, E. Maire, J. Lachambre, G. Martin, Fatigue performances of chemically etched thin struts built by selective electron beam melting: Experiments and predictions, Materialia 9 (2020), 100589, https://doi.org/10.1016/j.mtla.2020.100589.
[34] A. du Plessis, I. Yadroitsev, I. Yadroitsava, S.G. Le Roux, X-Ray microcomputed tomography in additive manufacturing: a review of the current technology and applications, 3D print, Addit. Manuf. 5 (2018) 227–247, https://doi.org/10.1089/3dp.2018.0060.
[35] A. du Plessis, S. Beretta, Killer notches: The effect of as-built surface roughness on fatigue failure in AlSi10Mg produced by laser powder bed fusion, Addit. Manuf. 35 (2020), 101424, https://doi.org/10.1016/j.addma.2020.101424.
[36] N. Sanaei, A. Fatemi, Defects in additive manufactured metals and their effect on fatigue performance: a state-of-the-art review, Prog. Mater. Sci. 117 (2021), 100724, https://doi.org/10.1016/j.pmatsci.2020.100724.
[37] S. Romano, A. Brückner-Foit, A. Brandão, J. Gumpinger, T. Ghidini, S. Beretta, Fatigue properties of AlSi10Mg obtained by additive manufacturing: defect-based modelling and prediction of fatigue strength, Eng. Fract. Mech. 187 (2018) 165–189, https://doi.org/10.1016/j.engfracmech.2017.11.002.
[38] H. Masuo, Y. Tanaka, S. Morokoshi, H. Yagura, T. Uchida, Y. Yamamoto, Y. Murakami, Influence of defects, surface roughness and HIP on the fatigue strength of Ti-6Al-4V manufactured by additive manufacturing, Int. J. Fatigue 117 (2018) 163–179, https://doi.org/10.1016/j.ijfatigue.2018.07.020.
[39] E. Pessard, M. Lavialle, P. Laheurte, P. Didier, M. Brochu, High-cycle fatigue behavior of a laser powder bed fusion additive manufactured Ti-6Al-4V titanium: Effect of pores and tested volume size, Int. J. Fatigue 149 (2021), 106206, https://doi.org/10.1016/j.ijfatigue.2021.106206.
[40] N. Sanaei, A. Fatemi, Defect-based fatigue life prediction of L-PBF additive manufactured metals, Eng. Fract. Mech. 244 (2021), 107541, https://doi.org/10.1016/j.engfracmech.2021.107541.
[41] Y. MURAKAMI, K. TAKAHASHI, T. YAMASHITA, Quantitative evaluation of the effect of surface roughness on fatigue strength. Effect of depth and pitch of roughness, Trans. Jpn. Soc. Mech. Eng. Ser. A 63 (1997) 1612–1619, https://doi.org/10.1299/kikaia.63.1612.
[42] Y. Lu, S. Wu, Y. Gan, T. Huang, C. Yang, L. Junjie, J. Lin, Study on the microstructure, mechanical property and residual stress of SLM Inconel-718 alloy manufactured by differing island scanning strategy, Opt. Laser Technol. 75 (2015) 197–206, https://doi.org/10.1016/j.optlastec.2015.07.009.
[43] S. Waqar, K. Guo, J. Sun, Evolution of residual stress behavior in selective laser melting (SLM) of 316L stainless steel through preheating and in-situ re-scanning techniques, Opt. Laser Technol. 149 (2022), 107806, https://doi.org/10.1016/j.optlastec.2021.107806.
[44] Q. Chen, H. Taylor, A. Takezawa, X. Liang, X. Jimenez, R. Wicker, A.C. To, Island scanning pattern optimization for residual deformation mitigation in laser powder bed fusion via sequential inherent strain method and sensitivity analysis, Addit. Manuf. 46 (2021), 102116, https://doi.org/10.1016/j.addma.2021.102116.
[45] A. Röttger, J. Boes, W. Theisen, M. Thiele, C. Esen, A. Edelmann, R. Hellmann, Microstructure and mechanical properties of 316L austenitic stainless steel processed by different SLM devices, Int. J. Adv. Manuf. Technol. 108 (2020) 769–783, https://doi.org/10.1007/s00170-020-05371-1.
[46] J. Bedmar, A. Riquelme, P. Rodrigo, B. Torres, J. Rams, Comparison of different additive manufacturing methods for 316L stainless steel, Materials 14 (2021) 6504, https://doi.org/10.3390/ma14216504.
[47] J.B.T.M. Roerdink, A. Meijster, The watershed transform: definitions, algorithms and parallelization strategies, Fundam. Inform. 41 (2000) 187–228, https://doi.org/10.3233/FI-2000-411207.
[48] J.H. Friedman, J.L. Bentley, R.A. Finkel, An algorithm for finding best matches in logarithmic expected time, ACM Trans. Math. Softw. 3 (1977) 209–226, https://doi.org/10.1145/355744.355745.
[49] G. Kovács, A. Fazekas, A. Hajdu, Exponential contrast maximization of intensity images, 7th Int. Symp. Image Signal Process. Anal. (ISPA) (2011) 139–142.
[50] C.A. Schneider, W.S. Rasband, K.W. Eliceiri, NIH Image to ImageJ: 25 years of image analysis, Nat. Methods 9 (2012) 671–675, https://doi.org/10.1038/nmeth.2089.
[51] R. Shrestha, J. Simsiriwong, N. Shamsaei, Fatigue behavior of additive manufactured 316L stainless stell parts: effects of layer orientation and surface roughness, Addit. Manuf. 28 (2019) 23–38, https://doi.org/10.1016/j.addma.2019.04.011.
[52] Y. Deng, Z. Mao, N. Yang, X. Niu, X. Lu, Collaborative optimization of density and surface roughness of 316L stainless steel in selective laser melting, Materials 13 (2020) 1601, https://doi.org/10.3390/ma13071601.
[53] D. Wang, Y. Liu, Y. Yang, D. Xiao, Theoretical and experimental study on surface roughness of 316L stainless steel metal parts obtained through selective laser melting, Rapid Prototyp. J. 22 (2016) 706–716.
[54] A. Hartman, J. Schijve, The effects of environment and load frequency on the crack propagation law for macro fatigue crack growth in aluminium alloys, Eng. Fract. Mech. 1 (1970) 615–631, https://doi.org/10.1016/0013-7944(70)90003-2.
[55] Y. Murakami, Metal Fatigue: effects of small defects and nonmetallic inclusions, Elsevier, 2002.
[56] A. Yadollahi, M.J. Mahtabi, A. Khalili, H.R. Doude, J.C. Newman, Fatigue life prediction of additively manufactured material: effects of surface roughness, defect size, and shape, Fatigue Fract. Eng. Mater. Struct. 41 (2018) 1602–1614, https://doi.org/10.1111/ffe.12799.
[57] A. Riemer, S. Leuders, M. Thöne, H.A. Richard, T. Tröster, T. Niendorf, On the fatigue crack growth behavior in 316L stainless steel manufactured by selective laser melting, Eng. Fract. Mech. 120 (2014) 15–25, https://doi.org/10.1016/j.engfracmech.2014.03.008.
[58] J.C. Newman, I.S. Raju, An empirical stress-intensity factor equation for the surface crack, Eng. Fract. Mech. 15 (1981) 185–192, https://doi.org/10.1016/0013-7944(81)90116-8.
[59] R. Jones, J.G. Michopoulos, A.P. Iliopoulos, R.K. Singh Raman, N. Phan, T. Nguyen, Representing crack growth in additively manufactured Ti-6Al-4V, Int. J. Fatigue 116 (2018) 610–622, https://doi.org/10.1016/j.ijfatigue.2018.07.019.
[60] A. Iliopoulos, R. Jones, J. Michopoulos, N. Phan, R. Singh Raman, Crack growth in a range of additively manufactured aerospace structural materials, Aerospace 5 (2018) 118, https://doi.org/10.3390/aerospace5040118.
[61] S.C. Wu, Z. Song, G.Z. Kang, Y.N. Hu, Y.N. Fu, The Kitagawa-Takahashi fatigue diagram to hybrid welded AA7050 joints via synchrotron X-ray tomography, Int. J. Fatigue 125 (2019) 210–221, https://doi.org/10.1016/j.ijfatigue.2019.04.002.
[62] S.C. Wu, C. Yu, P.S. Yu, J.Y. Buffière, L. Helfen, Y.N. Fu, Corner fatigue cracking behavior of hybrid laser AA7020 welds by synchrotron X-ray computed microtomography, Mater. Sci. Eng. A. 651 (2016) 604–614, https://doi.org/10.1016/j.msea.2015.11.011.
[63] P. Li, P.D. Lee, T.C. Lindley, D.M. Maijer, G.R. Davis, J.C. Elliott, X-ray microtomographic characterisation of porosity and its influence on fatigue crack growth, Adv. Eng. Mater. 8 (2006) 476–479, https://doi.org/10.1002/adem.200600051.
[64] A. Yadollahi, M.J. Mahtabi, A. Khalili, H.R. Doude, J.C. Newman, Fatigue life prediction of additively manufactured material: effects of surface roughness, defect size, and shape, Fatigue Fract. Eng. Mater. Struct. 41 (2018) 1602–1614, https://doi.org/10.1111/ffe.12799.

[65] M. Kamaya, Growth evaluation of multiple interacting surface cracks. Part I: experiments and simulation of coalesced crack, Eng. Fract. Mech. 75 (2008) 1336–1349, https://doi.org/10.1016/j.engfracmech.2007.07.015.
[66] X.B. Lin, R.A. Smith, A numerical simulation of fatigue growth of multiple surface initially semicircular defects under tension, Int. J. Press. Vessel. Pip. 62 (1995) 281–289, https://doi.org/10.1016/0308-0161(94)00021-A.
[67] J.H.L. Pang, H.J. Hoh, K.S. Tsang, J. Low, S.C. Kong, W.G. Yuan, Fatigue crack propagation analysis for multiple weld toe cracks in cut-out fatigue test specimens from a girth welded pipe, Int. J. Fatigue 94 (2017) 158–165, https://doi.org/10.1016/j.ijfatigue.2016.09.011.